



Microstructure and residual stress evolution in nanocrystalline Cu-Zr thin films



J. Chakraborty^{a,*}, T. Oellers^b, R. Raghavan^c, A. Ludwig^b, G. Dehm^d

^a Materials Engineering Division, National Metallurgical Laboratory, Council of Scientific and Industrial Research, P.O. Burmahines, Jamshedpur 831007, India

^b Chair for Materials Discovery and Interfaces, Institute for Materials, Ruhr University, 44801 Bochum, Germany

^c Department of Materials Engineering, Indian Institute of Science, Bangalore 560012, India

^d Department of Structure and Nano-/Micromechanics of Materials, Max-Planck-Institut für Eisenforschung GmbH, Max-Planck-Strasse 1, Dusseldorf 40237, Germany

ARTICLE INFO

Article history:

Received 3 August 2021

Received in revised form 12 November 2021

Accepted 13 November 2021

Available online 24 November 2021

Keywords:

X-ray diffraction

Cu-Zr

Thin films

Microstructure

Residual stress

ABSTRACT

Grazing incidence X-ray diffraction (GIXRD) and scanning transmission electron microscopy (STEM) combined with energy dispersive X-ray spectroscopy (EDS) were employed to study the microstructure evolution and stress development in the nanocrystalline $\text{Cu}_{100-x}\text{Zr}_x$ ($2.5 \text{ at}\% \leq x \leq 5.5 \text{ at}\%$) alloy thin films. Small Zr additions to Cu led to significant lattice parameter anisotropy in the as-deposited Cu-Zr thin films both due to macroscopic lattice strain and stacking faults in the Cu matrix. Strain free lattice parameters obtained after the XRD stress analysis of Cu-Zr thin films confirmed formation of a supersaturated substitutional Cu-Zr solid solution. For the first time, the study of film microstructure by XRD line profile analysis (XLP) confirmed progressive generation of dislocations and planar faults with increasing Zr composition in Cu-Zr alloy films. These microstructural changes led to the generation of tensile stresses in the thin films along with considerable stress gradients across the films thicknesses which are quantified by the traditional $d_{\psi}^{hk\ell} - \sin^2 \psi$ and GIXRD stress measurement methods. The origin of tensile stresses and stress gradients in the Cu-Zr film are discussed on the basis of film growth and heterogeneous microstructure with changing Zr composition.

© 2021 Published by Elsevier B.V.

1. Introduction

Nanocrystalline Cu (grain size < 100 nm) exhibits remarkably high mechanical strength [1–3]. However, the large volume fraction of grain boundaries in this nanocrystalline metal produces a high driving force for grain growth at temperature as low as 75 °C [4]. This leads to grain growth and a resulting degradation of mechanical properties [4–6]. Hence, the microstructural instability of nanocrystalline metals is a major concern for their practical applications [4–10]. Interestingly, a small Zr addition (i.e. < 1 at%) to nanocrystalline Cu successfully stabilizes the microstructure against grain growth even at temperature as high as 800 °C [11–13]. The equilibrium phase diagram of Cu-Zr system shows that Cu and Zr have very limited mutual solid solubility (maximum solubility of Zr in Cu is 0.12 at% at the eutectic temperature 1245 K) due to large atomic

size mismatch between Cu and Zr atoms (~ 24%) and Zr atoms have a strong tendency to segregate in the Cu grain boundaries [14,15]. Segregation of Zr atoms at the Cu grain boundaries causes significant reduction of the grain boundary energy from 0.6 J/m² (pure Cu) to 0.2 J/m² (after Zr segregation [16]) which reduces grain growth propensity in nanocrystalline Cu [11,16]. In this context, it is important to note that the maximum concentration of Zr atoms segregating at the Cu grain boundaries cannot exceed 0.5 at% due to the positive dipole interaction energy of Zr solute with Cu (~ 0.29 eV) (i.e. Zr atoms repel each other) [17].

In recent years, the concept of small Zr additions has been employed to stabilize nanocrystalline Cu and several efforts have been made to further extend the solid solubility between Cu and Zr atoms by synthesizing nanocrystalline Cu-Zr alloys in the Zr composition range between 0.1 at% and 8 at% using various non-equilibrium synthesis methods such as mechanical alloying [11,18–20], physical vapor deposition [16,21–24] and severe plastic deformation (SPD) methods [25–28]. Thermodynamically, during the synthesis of nanocrystalline Cu-Zr alloys under non-equilibrium conditions, the necessary Gibbs free energy to extend the solubility between Cu and

* Corresponding author.

E-mail addresses: jay@nmlindia.org (J. Chakraborty), tobiasoellers@gmail.com (T. Oellers), rejnr@gmail.com (R. Raghavan), alfred.ludwig@rub.de (A. Ludwig), dehm@mpie.de (G. Dehm).

Zr (otherwise immiscible at equilibrium) comes from the excess energy stored at the grain boundaries /interfaces and increased elastic strain energy due to lattice defects (dislocations) [18,29] and elastic stresses especially in case of Cu-Zr thin films on a rigid substrate [30–32]. However, despite several investigations on Cu-Zr nanocrystalline alloys, experimental results obtained until now are inconclusive, particularly concerning the solid solubility limit of Zr in nanocrystalline Cu and the Zr alloying effects on the microstructure of Cu matrix. For example, Azimi and Akbari [18] reported formation of a supersaturated Cu-Zr solid solution up to 6 at% Zr by ‘mechanical alloying’ of Cu and Zr powders. However, Atwater et al. [11] have found extensive formation of intermetallic phase for both 2 at% and 5 at% Zr content in the Cu-Zr alloys prepared by mechanical alloying. Alloys containing 1 at% Zr showed segregation of Zr atoms at Cu grain boundaries along with small amount of intermetallic phase formation. In case of magnetron sputtered room temperature deposited Cu-Zr thin films having Zr content ranging from 0.4 at% to 7 at%, grain boundary segregation of Zr atoms occurred up to 1 at% Zr and amorphous phase formed at the Cu grain boundaries for ≥ 3 at% Zr [21]. Similarly, magnetron sputtered and vacuum annealed Cu-Zr thin films (i.e. microstructure stabilized films) revealed Zr segregation up to 0.5 at% Zr composition and amorphous phase formation at the Cu grain boundaries for ≥ 2 at% Zr [16]. On the other hand, Oellers et al. recently reported complete solid solubility between Cu and Zr atoms up to 5.5 at% Zr in room temperature magnetron sputtered Cu-Zr thin films without any evidence of Zr segregation [24].

Interestingly, Zr addition to nanocrystalline Cu produced significant microstructural changes resulting in improved mechanical properties of nanocrystalline Cu-Zr alloys [16,21,24]. In addition, mechanically alloyed nanocrystalline Cu-Zr powder with 1 at%, 2 at% and 5 at% Zr exhibited excellent grain size stability up to 800 °C for 1 h [11]. Considerable grain refinement and nanotwinning in the Cu matrix was reported in sputtered Cu-Zr thin films [16,21]. Oellers et al. [24] showed significant grain size refinement in the Cu-Zr thin films with increasing Zr content but did not observe grain boundary segregation of Zr. From a thermodynamic viewpoint, nanocrystalline Cu-Zr alloy thin films form twins due to the lowering of stacking fault energy (SFE) of the Cu matrix upon Zr addition from 0.4 at% to 8 at% [33,34]. Such lowering of SFE of Cu also occurs due to addition of Zn [35–38], Sn [35] and Al [39] as well. However, SFEs of Cu-Zr alloys with such low Zr content are not available in the literature. Lowering of SFE can change the plastic deformation mechanism and extent of grain size refinement of Cu-Zr alloy thin films as observed in nanocrystalline Cu-Zn alloys obtained by high pressure torsion [38] and cold rolled and isothermally annealed Cu–15 at% Al alloy [40]. Grain refinement in severely plastically deformed bulk Cu based fcc alloys has been studied extensively [40–43].

Microstructural changes in nanocrystalline Cu-Zr thin films could also cause changes in residual stresses in the films with varying Zr contents and micro/nanostructure heterogeneity could lead to stress gradients in the thin films. To the best of our knowledge, residual stress generation and its variation in Cu-Zr thin films as a function of Zr content has not been investigated. In view of the above considerations, the present work investigates the effects of Zr alloying on the evolution of phase, defect microstructure, and residual stresses in nanostructured $\text{Cu}_{(100-x)}\text{Zr}_x$ thin films (2.5 at% $\leq x \leq 5.5$ at%) by detailed X-ray diffraction (XRD) and scanning transmission electron microscopy (STEM) investigations. Preliminary microstructure, crystallographic texture and mechanical properties of these Cu-Zr thin films were reported by Oellers et al. [24]. In this study, XRD line profile analysis (XLPA) of Cu-Zr thin films was carried out in order to understand the evolution of lattice defects such as dislocations and planar faults due to Zr alloying of Cu in Cu-Zr thin films with 2.5 at% to 5.5 at% Zr. Further qualitative evidence and nature of these lattice defects were derived from the detailed analysis of the lattice parameter data obtained from the GIXRD results of

Cu-Zr thin films. The role of XLPA derived dislocations and planar faults in the grain refinement of Cu-Zr thin films were studied as a function of Zr composition. Residual stress generation and possible presence of stress gradient in Cu-Zr thin films were investigated by traditional XRD and GIXRD stress measurements respectively.

2. Experimental procedure

2.1. Preparation and chemical compositions of Cu-Zr alloy thin films

Polycrystalline $\text{Cu}_{100-x}\text{Zr}_x$ (2.5 at% $\leq x \leq 5.5$ at%) alloy thin films (thickness $\sim 2 \mu\text{m}$) were deposited at room temperature on thermally oxidized Si(100) wafers by simultaneous sputtering of two diametrically opposite Cu targets and a single Zr target in a magnetron sputtering chamber. Thin film deposition parameters, procedures and film thickness measurements were reported in detail by Oellers et al. [24]. Chemical compositions of the as-grown thin films were obtained by energy dispersive X-ray spectroscopy (EDS) using a Jeol JSM-5800LV scanning electron microscope (SEM) with an Oxford instruments INCA * X-act EDS detector (see Ref. [24] for more details).

2.2. Structural characterization

The as-deposited Cu-Zr thin films were characterized by grazing incidence XRD (GIXRD) for phase analysis using $\text{Co-K}\alpha$ radiation in a Seifert Diffractometer (ID3003) equipped with parallel beam optics, an Eulerian cradle and an energy dispersive X-ray detector (Meteor OD). An incidence angle of 2° was used while scanning over the angular range of 30° to 130° (2θ) with 0.05° step width and 30 s time/step. Measured XRD patterns were fitted with Pearson-VII functions using a peak fitting program (PROFIT, PANalytical) [44] in order to determine the peak parameters (i.e. peak maximum position, FWHM (full width at half maxima), integral breadth etc.) corresponding to $\text{K}\alpha_1$ radiation. Obtained peak parameters were used to carry out the XRD line profile analysis (XLPA) for determining the average crystallite sizes (i.e. size of coherently diffracting domains), lattice defects (i.e. dislocations and planar faults) and micro-strains (i.e. inhomogeneous strain) in the Cu-Zr films. Instrumental correction was done using standard CeO_2 powder (strain free and grain size $> 1 \mu\text{m}$) specimen from ‘National Institute of Standards and Technology (NIST)’. Detailed methodology of the microstructural characterization of Cu-Zr thin films was outlined in Section 2.3 and also in the supplementary material. Additionally, the film microstructure was also studied by transmission electron microscopy (TEM) (see Ref. [24] for details).

Furthermore, in order to measure the residual stresses in Cu-Zr alloy films, macroscopic strain measurements were carried out by measuring orientation dependent inter-planar lattice spacing (d_ψ^{hkl}) corresponding to {111} reflection of the fcc Cu-Zr alloy thin films at various specimen tilt angles (ψ) (i.e. angle between the specimen surface normal and the diffraction vector). Diffraction stress analysis was performed by the traditional $d_\psi^{hkl} - \text{Sin}^2\psi$ method [45]. For a rotationally symmetric plane state of stress (measurements at rotation angles $\varphi = 0^\circ$ and $\varphi = 90^\circ$ yield the same stress value σ), the stress σ can be determined from the following equation [45]:

$$d_\psi^{hkl} = \frac{1}{2} S_2^{hkl} d_0^{hkl} \sigma \text{Sin}^2\psi + (1 + 2S_1^{hkl} \sigma) d_0^{hkl} \quad (1)$$

where d_0^{hkl} is the strain free inter-planar lattice spacing of the {hkl} planes. S_1^{hkl} and $(1/2)S_2^{hkl}$ are the so-called X-ray elastic constants (XECs) [45]. Neerfield-Hill (N-H) average XECs of pure Cu phase were calculated from the single crystal elastic constants of Cu [46] using the Voigt and Reuss models [45] assuming that the elastic properties of Cu (Zr) do not change significantly with such small Zr addition (up to 5.5 at%). Table 1 shows N-H average XECs for {111} reflections.

Table 1
Neerfield-Hill Average XECs for polycrystalline Cu.

Cu reflections	$(1/2)S_2^{hkl}$ (10^{-11} Pa $^{-1}$)	S_1^{hkl} (10^{-11} Pa $^{-1}$)
{111}	0.792	- 0.184
{200}	1.49	- 0.45
{220}	1.0	- 0.25
{311}	1.18	- 0.313
{222}	0.792	- 0.184

Strain free inter-planar lattice spacings for the Cu-Zr alloy thin films were determined from the measured $d_{\psi}^{hkl} - \sin^2 \psi$ plots following a procedure published elsewhere [45,47,48]. Eq. (1) shows that the stress (σ) can be calculated from the slope of the straight line fitted to the $d_{\psi}^{hkl} - \sin^2 \psi$ plot.

In addition to aforementioned traditional $d_{\psi}^{hkl} - \sin^2 \psi$ method, residual stresses in Cu-Zr alloy thin films were also measured in the GIXRD geometry [45,47,49]. During stress measurement, the angle of incidence of X-ray (α) was kept fixed (and kept small $\alpha = 1^\circ, 2^\circ$ and 3°) and several hkl diffraction lines were recorded by 2θ scan in the GIXRD mode. Therefore, for a fixed angle of incidence (α), the X-ray penetration depth within the thin film remains almost constant. However, due to fixed angle of incidence (α), there is a dependence between the Bragg angle (θ^{hkl}) and the specimen tilt angle (ψ) (see Fig. 1). In this case, for a set of $\{hkl\}$ diffraction planes, the specimen tilt angle (ψ) (i.e. angle between the specimen normal and the diffraction vector) is given by

$$\psi = \theta^{hkl} - \alpha \quad (2)$$

Therefore, during GIXRD stress measurement, by measuring the lattice strains using different

hkl reflections (i.e. different θ^{hkl}), the direction of lattice strain measurement can be varied without even physically tilting the specimen in the diffractometer. Stress analysis in the GIXRD mode was performed using the so-called $f(\psi, hkl)$ method [47,49] for a rotationally symmetric biaxial state of stress which is described as follows:

$$\varepsilon_{\psi}^{hkl} = f(\psi, hkl) < \sigma > \quad (3)$$

$$\varepsilon_{\psi}^{hkl} = \frac{a_{\psi}^{hkl} - a_0}{a_0} \quad (4)$$

and

$$f(\psi, hkl) = 2S_1^{hkl} + \frac{1}{2}S_2^{hkl}\sin^2 \psi \quad (5)$$

The inter-planar lattice spacing (d_{ψ}^{hkl}) was converted into lattice parameter (a_{ψ}^{hkl}) in order to avoid the problem of many d_{ψ}^{hkl} values for different hkl reflections. Strain (ε_{ψ}^{hkl}) can be determined for several hkl reflections for different (hypothetical) ψ tilt angles and the plot of ε_{ψ}^{hkl} versus $f(\psi, hkl)$ can be fitted with a straight line. Stress (σ) can be determined from the slope of the straight line with a_0^{hkl} is the fitting parameter. The Neerfield-Hill XECs corresponding to {111}, {200},

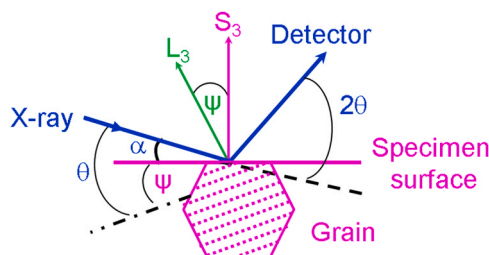


Fig. 1. Schematic of GIXRD stress measurement using multiple hkl reflections. The diffraction vector (L_3) is denoted as \vec{g} in the text.

{220}, {311} and {222} reflections have been presented in Table 1 [45,46].

2.3. X-ray diffraction line profile analysis: evaluation of microstructural parameters

Detailed analysis of the broadening of XRD line profiles was carried out by the so-called Williamson-Hall (W-H) [50] and modified Williamson Hall (MWH) [51] methods in order to evaluate various microstructural parameters (i.e. crystallite size (D), dislocation density (ρ), dislocation types (screw/edge), planar fault probability (β), and microstrain (ϵ)) in the Cu-Zr thin films. Detailed method of size and strain separation by the W-H and the MWH procedures are outlined in the supplementary material SM.1. The MWH plots were constructed in order to confirm dislocation induced anisotropic microstrain broadening of XRD line profiles of Cu-Zr thin films. Furthermore, possible presence of planar faults in the Cu-Zr crystallites and their effects on the peak broadening was examined by taking account of the so-called contrast factors of planar faults ($\Delta K - \beta W(g)$) for different reflections (or diffraction vectors, \vec{g}) [52] (see supplementary material SM.1). The diffraction peak broadening caused by dislocations depends on the relative orientations of the Burgers vector (b) and the diffraction vector (\vec{g}). This effect is taken into account by the average dislocation contrast factor (\bar{C}). SM.2 provides the method for calculation of (\bar{C}) for cubic crystal system using a computer code ANIZC developed by Ungar et al. [51,53–60]. The calculated values of \bar{C} for both pure edge and pure screw dislocations for individual diffraction vector (\vec{g}) are presented in Table 3. For faults in the fcc crystals, $W(g)$ for different hkl reflections determined by Warren [52] are presented in Table 3. Data points in the MWH plot (i.e. plot of $(\Delta K - \beta W(g))$ vs. $K\bar{C}^{1/2}$; see Eq. (4) in the supplementary material SM.1 where $K = \frac{2\sin\theta}{\lambda}$ (i.e. $\Delta K (FWHM) = 2\cos\theta(\Delta\theta)/\lambda$; θ and λ are the diffraction angle and the wavelength of X-rays respectively [51,53]) were fitted by a quadratic curve using a least square fitting routine in order to determine various fitting parameters. These fitting parameters were used to determine the volume averaged size of the coherently diffracting domains (i.e. crystallite size), average dislocation density, dislocation character (screw/edge), planar fault probability and the microstrain in Cu-Zr alloy thin films. Additionally, an approximate method [61–63] of dislocation density determination from the fitting parameter has been described in SM.3.

3. Results and interpretation

3.1. Phase analysis and lattice parameter determination

Fig. 2(a) shows a typical GIXRD pattern of the polycrystalline Cu - 4.5 at% Zr thin film where the prominent Bragg peaks were indexed with respect to fcc Cu phase. A magnified plot of the GIXRD patterns in a limited 2θ region presented in Fig. 2(b) shows a gradual shift of {111} and {200} Cu reflections towards lower 2θ side (i.e. higher $d_{\{hkl\}}$ or higher $a_{\{hkl\}}$) with increasing Zr composition. This qualitatively indicates lattice expansion due to Zr incorporation in the Cu matrix. Additionally, broadening of the diffraction peaks is evident in the GIXRD pattern (Fig. 2(a)). The broadening increases with increasing Zr content (Fig. 2(b)). Qualitatively, diffraction peak broadening indicates presence of nanometer sized crystallites and/or large microstrain or inhomogeneous strain due to lattice defects. The lattice parameters ($a_{\{hkl\}}$) were calculated from the peak maximum positions (2θ) of different hkl reflections in the GIXRD patterns using Bragg's law ($a_{\{hkl\}} = \lambda\sqrt{(h^2 + k^2 + l^2)}/2\sin\theta$), taking account of the errors in the 2θ values up to fourth decimal places. Fig. 2(c) shows so-called 'Cohen-Wagner plots' [64,65] for Cu-Zr thin films up to 4.5 at% Zr composition. Large broadening and weak intensities of

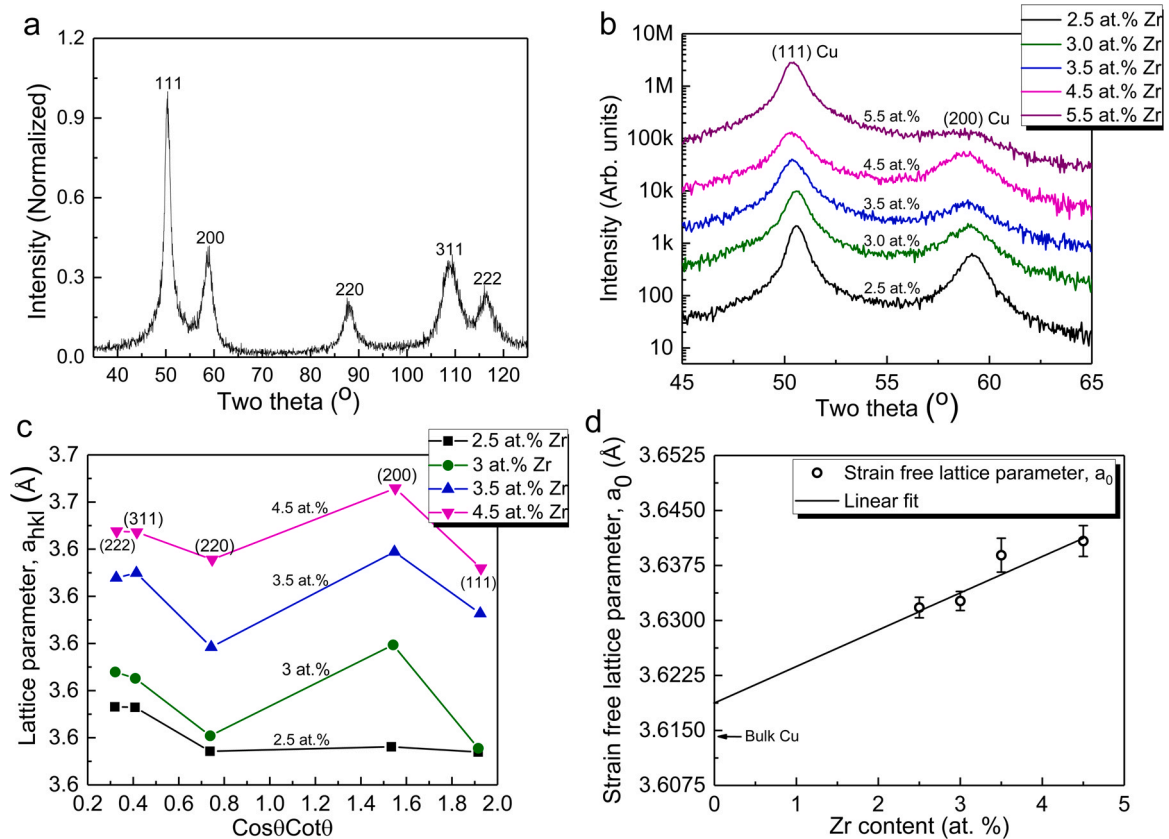


Fig. 2. (a) GIXRD pattern of Cu-4.5 at% Zr thin film; (b) Magnified plot of the GIXRD pattern in a limited 2θ range shows the relative shift of {111} Cu and {200} Cu diffraction peaks as a function of Zr composition in the as deposited thin films; (XRD data is replotted from [24]) (c) Lattice parameter anisotropy in Cu-Zr thin films as a function of Zr composition. Strain free lattice parameters for various Zr compositions (for comparison): (i) 3.63176 ± 0.0014 Å at 2.5 at% Zr, (ii) 3.63266 ± 0.0013 Å at 3 at% Zr; (iii) 3.6389 ± 0.0023 Å at 3.5 at% Zr & (iv) 3.64083 ± 0.0021 Å for 4.5 at% Zr. Lattice parameter for 5.5 at% Zr could not be determined; (d) Strain free lattice parameters of Cu-Zr thin films plotted as a function of Zr composition (lattice parameter data is replotted from [24]).

some of the diffraction peaks made the lattice parameter values of the Cu-5.5 at% Zr thin film uncertain. It is clear that the measured lattice parameters (a_{hkl}) of the Cu-Zr thin films increase with increasing Zr content (see Fig. 2(c)). Furthermore, a general observation of lattice parameter anisotropy (i.e. pronounced hkl dependence of a_{hkl} ; for example, $a_{\{111\}} < a_{\{200\}}$ and $a_{\{111\}} < a_{\{222\}}$, $a_{\{311\}}$ in general) is evident from the Cohen-Wagner plots for all Zr compositions. Such pronounced lattice parameter anisotropy prevents least square fitting of straight lines to the data points in the Cohen-Wagner plots and therefore, precise lattice parameter determination for each Cu-Zr composition was not possible. Observed lattice parameter anisotropy may have mainly the following origins: (i) macroscopic lattice strains (elastic strains due to intrinsic film stress) in thin film and their effects on the measured lattice parameter values (a_{hkl}) can have pronounced hkl dependence due to significant elastic anisotropy of Cu (anisotropic Young's modulus and Poisson's ratio); (ii) randomly distributed stacking faults on the {111} lattice planes in fcc Cu matrix due to Zr addition which leads to pronounced hkl dependent shift of the diffraction peak positions of Cu and hence the lattice parameters (a_{hkl}). The effect of extended and non-interacting stacking faults on the lattice parameters of an untextured polycrystalline metal is characterized by the contrast factors (G_{hkl}) for stacking faults calculated by Warren [52, 66–68] for various reflections (Table 2). The effect of compositional strain (i.e. elastic strain due to atomic size mismatch between Zr and Cu atoms) on the lattice parameter anisotropy of fcc Cu was assumed to be negligible. Additional assumptions include isotropic diffusion of Zr in a Cu crystallite/grain and homogeneous Zr distribution in all Cu-Zr crystallites.

Table 2

Contrast factors of stacking faults (G_{hkl}) on {111} planes in fcc metals. The values of cubic invariants are presented in the last column.

{h k l}	G_{hkl}	$(h^2k^2 + k^2l^2 + h^2l^2)/(h^2 + k^2 + l^2)^2$
{111}	- 0.25	0.33
{200}	0.5	0
{220}	- 0.25	0.25
{311}	0.09	0.157
{222}	0.125	0.33

In order to determine the lattice parameter variation on the Zr content, 'strain-free lattice parameters' (a_0) were determined from the XRD stress measurements of the Cu-Zr thin films (Section 2.2 and Refs. [44,46,47] provide detailed methodology). Such 'strain-free lattice parameter' of a Cu-Zr thin film refers to the average lattice parameter of those crystallites which are free from all macroscopic stresses/strains and lattice defects in the film except the compositional strain. The linear increase of strain-free lattice parameters with increasing Zr content (see Fig. 2(d)) suggests expansion of Cu lattice due to Zr addition in the form of random non-equilibrium substitutional solutes. This lattice expansion in Cu-Zr thin films was also briefly mentioned by Oellers et al. [24] and at present it is being investigated in detail. The data points in Fig. 2(d) can be fitted by a straight line. An extrapolation to pure Cu at zero at% Zr results in a lattice parameter value of $\sim (3.6188 \pm 0.0041)$ Å whereas pure fcc Cu has a lattice parameter value of 3.6149 Å [69]. In this context, it is noteworthy that possible tetragonal distortion of the fcc unit cell was excluded since the XRD patterns of Cu-Zr thin films did not exhibit clear evidence of splitting of 200, 220 and 311 reflections.

Next, the measured values of the lattice parameters $a_{\{hkl\}}$ plotted in Fig. 2(c) were compared to the corresponding strain free lattice parameter (a_0) value for each Cu-Zr composition in order to understand the effect of macroscopic lattice strains and the planar defects such as stacking faults (if any) on the observed lattice parameter anisotropy (Fig. 2(c)). Interestingly, this comparison revealed that the lattice parameters for {200}, {311} and {222} diffraction planes increased for all Cu-Zr compositions whereas those for the {111} and {220} planes decreased for all except Zr contents > 3 at%. Additionally, notable differences between the lattice parameters of {111} and {222} diffraction planes (i.e. $(a_{222} - a_{111}) > 0$) were observed for all Cu-Zr thin films (Fig. 2(c)). In general, such lattice parameter $a_{\{hkl\}}$ variation with the diffraction indices hkl qualitatively indicates presence of stacking faults on the {111} planes of fcc Cu matrix due to Zr incorporation, in addition to large macroscopic lattice strains in the films [52, 64–66]. The stacking fault contrast factors ($G_{\{hkl\}}$) (see Table 2) indicate that an increase of stacking fault probability (α) on {111} planes will increase the lattice parameters calculated from {200}, {311} and {222} planes and decrease the lattice parameter deduced from {111} and {220} planes systematically as compared to the strain free lattice parameter since lattice strain due to stacking faults is $\sim(\sqrt{3}/4\pi)\alpha G_{\{hkl\}}$ [52, 64–68].

The observation of $(a_{222} - a_{111}) > 0$ was also attributed to stacking faults since $G_{111} = -0.25$ and $G_{222} = 0.125$ (see Table 2) and not to macroscopic lattice strains. Interestingly, the difference between a_{222} and a_{111} is decreased at Zr contents > 3 at% which probably suggests reduced influence of stacking faults on the lattice parameters. The observed increase of the lattice parameters for {111} and {220} planes at higher Zr contents (> 3 at%), (i.e. deviation from the Warren model) may be due to the presence of large macroscopic lattice strains in the Cu-Zr thin films. In case of macroscopic elastic strain, the hkl dependence of lattice parameter is governed by the so called 'cubic invariants' obtained from: $(h^2k^2 + l^2k^2 + h^2l^2)/(h^2 + k^2 + l^2)^2$ [66,70]. The {111} lattice planes possess the highest value of the cubic invariant of ~ 0.33 followed by {220} planes with ~ 0.25 (Table 2) and hence the lattice parameters for both these planes should be affected the most. Literature reported lattice parameter anisotropy due to the presence of stacking faults exists in case of deformed bulk Cu-Zn and Cu-Sn alloys [35,71]. However, the effect of Zr segregation to the stacking faults on the diffraction peak positions/lattice parameter variation is neglected due to lack of evidence from the XRD line profiles of Cu-Zr thin films.

3.2. XRD analysis of microstructure of Cu-Zr thin films

Conventional Williamson-Hall (W-H) plots for the Cu-Zr thin films are presented in Fig. 3(a) where the FWHMs for the first five reflections are plotted with the order of reflection (i.e. $\sin\theta$; $K=2\sin\theta/\lambda$) for each Zr composition. The W-H plots reveal non-monotonic increase of FWHMs with K indicating anisotropic (i.e. considerable hkl dependence) strain broadening mainly due to dislocations in the Cu-Zr alloy thin films. Similar behavior of the W-H plot was reported for cold worked Pb-Bi alloys [57], ball milled Fe powders [62], ball milled Ti powders [63] and also for severely plastically deformed Cu [72] in which the lattice strains were entirely due to dislocations. Fig. 3(a) also shows that FWHMs of {200}, {220} and {222} reflections have a decreasing trend with K in general. Furthermore, almost identical slopes of the lines joining these reflections in the W-H plots up to 3.5 at% Zr composition indicates the same dislocation character (screw/edge) in the Cu-Zr films up to 3.5 at% Zr. Hence, the slope change beyond 3.5 at% Zr indicates a change in the dislocation character in the Cu-Zr films with increasing Zr concentration.

In order to understand the root cause of such anisotropic strain broadening observed from the W-H plots, the so called 'modified

Williamson-Hall (MWH) plots' were constructed (see Fig. 3(b)) taking account of the presence of dislocations along with a finite probability (β) of planar faults (if any) in the films. In the MWH plots (Fig. 3(b)) the FWHMs (ΔK) plotted earlier in the 'y' axis of the W-H plot (i.e. Fig. 3(a)) have been replaced by $\Delta K - \beta W(g)$ and plotted as a function of $K\bar{C}^{1/2}$ where \bar{C} is the average contrast factor of dislocations for a particular reflection (i.e. diffraction vector). The details of the MWH analysis approach are discussed in Section 2.3 (also see supplementary material). Table 3 shows the average contrast factors of pure edge and pure screw dislocations for different diffraction vectors and a list of scaling factors $K\bar{C}^{1/2}$ for different diffraction vectors are presented in Table 3 for pure screw, pure edge and (50% screw + 50% edge) dislocations. Table 3 also shows the contrast factors ($W(g)$) of the planar faults for different diffraction vectors for the fcc crystal [52,53]. The MWH plot were fitted by a second order polynomial using a least square fitting algorithm in order to determine the various fitting parameters described in the supplementary material. The best fit was obtained when $\Delta K - \beta W(g)$ is plotted against a particular set of $K\bar{C}^{1/2}$ values calculated from a fixed proportion of edge and screw dislocations with a finite probability of planar faults (β) with appropriate contrast factors ($W(g)$) provided in Table 3. The planar fault probability (β) is a fitting parameter which is determined by fitting the MWH plot. For example, a combination of '90% screw + 10% edge' dislocations and a planar fault probability of 0.014 gave the best fit for the MWH plot in Cu-3.5 at% Zr thin film (Fig. 3(b)). In this context, it is noteworthy that the MWH plots can also be fitted assuming absence of planar faults in the Cu-Zr thin films (i.e. $\beta = 0$). Fig. 3(c-1) & 3(c-2) show the influence of β on the quality of data fitting in the MWH plot for Cu-3.5 at% Zr thin film.

Fig. 3(d) shows the variation of screw dislocation percentage as a function of Zr composition and interestingly the dislocations were screw in character up to 3.5 at% Zr which was predicted earlier from the W-H plots. This is further confirmed from the 'q' value determined from the ratio of the slope and the intercept of the straight line fitted to the plot of $(\Delta K)^2/K^2$ Vs H^2 in Fig. 3(e) (Refs. [56–58] & supplementary material SM.2 contain details). The values of 'q' are 2.135, 2.033 and 2.12 for Zr composition 2.5 at%, 3 at% and 3.5 at% respectively which indicates that the dislocations are predominantly screw in character up to 3.5 at% Zr composition. The theoretical value of parameter 'q' corresponding to 100% screw dislocations is 2.473 [56–58]. A lower q value of 1.7 indicates the presence of edge dislocations in the films with 4.5 at% Zr.

The average crystallite size (i.e. size of the coherently diffracting domains along the diffraction vector) calculated from the fitting parameter of the MWH plot decreased by almost 90% with increasing Zr composition with the lowest average crystallite size ~ 13 nm for 4.5 at% Zr (Fig. 4(a)) which indicates that Zr acts as a grain refiner in the Cu-Zr thin films [24]. Interestingly, such a decrease of crystallite size is associated with an increase of planar fault probability in Cu-Zr thin films which was indeed observed with increasing Zr content in Cu-Zr alloy thin films (Fig. 4(b)).

Fig. 4(c) shows an increase of average dislocation density up to 3.5 at% Zr by a factor of ~ 3 , but drops back by a factor of ~ 2.5 beyond in the Cu-Zr thin films. On the other hand, the microstrain increases rapidly by a factor of ~ 2 up to 3.5 at% Zr and then practically remained constant up to 5.5 at% Zr in the Cu-Zr thin films (Fig. 4(d)). Table 4 summarizes the Zr composition dependent crystallite size, average dislocation density and dislocation character in Cu-Zr thin films. Finally, it is noteworthy that diffraction line broadening arising due to compositional heterogeneity in the Cu-Zr crystallites was neglected as the Zr was assumed to be homogeneous in the Cu-Zr crystallites in all Cu-Zr thin films. Furthermore, compositional broadening is known to be isotropic in cubic crystals [73,74].

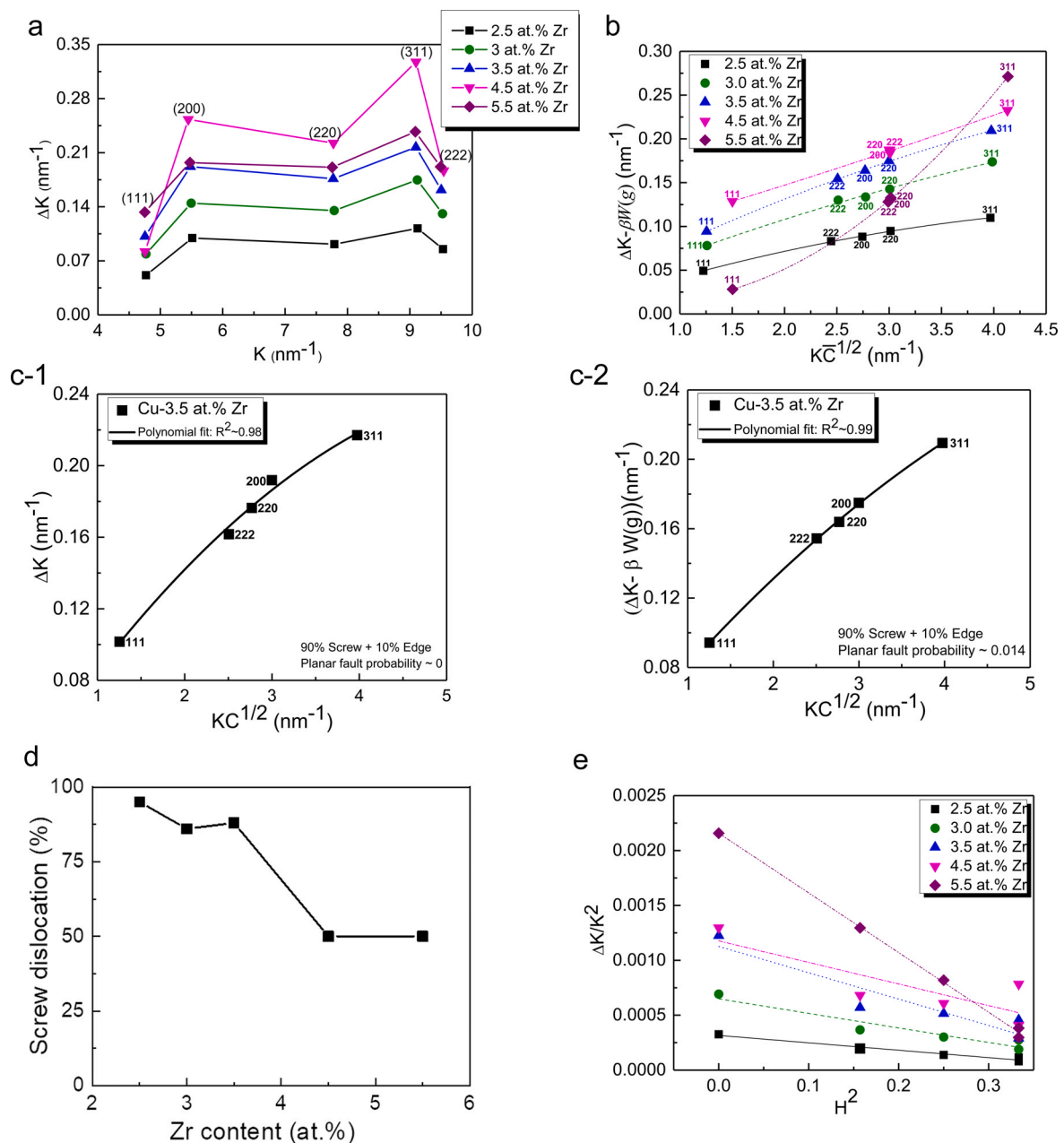


Fig. 3. (a) Williamson-Hall plot for the Cu-Zr alloy thin films; (b) Modified Williamson-Hall plots for Cu-Zr alloy thin films; (c-1) data points in MWH plot fitted with zero planar fault probability ($\beta = 0$) & (c-2) fitted with $\beta = 0.014$ for Cu-3.5 at% Zr thin film; (d) Variation of screw dislocations in the Cu-Zr alloy films as a function of Zr composition; (e) Plot of $(\Delta K/K)^2$ Vs H^2 for the determination of 'q' value (see text) in Cu-Zr alloy thin films.

Table 3

Average contrast factors (\bar{C}) for different vectors (\vec{g}) and values of $KC^{1/2}$ for pure edge, pure screw and ("50% screw + 50%edge") dislocation distribution for Cu-Zr thin films having 4.5 at% Zr. Contrast factors of planar faults for peak broadening ($W(\vec{g})$) in fcc crystals are also presented.

\vec{g}	$\bar{C}_{hkl \text{ pure edge}}$	$\bar{C}_{hkl \text{ pure screw}}$	$KC^{1/2}_{\text{screw}}$	$KC^{1/2}_{\text{edge}}$	$KC^{1/2}_{(50\% \text{ screw} + 50\% \text{ edge})}$	$W(\vec{g})$
{111}	0.138	0.062	1.18304	1.76308	1.50134	0.43
{200}	0.304	0.298	2.9913	3.02105	3.00621	1
{220}	0.179	0.121	2.69942	3.28526	3.00664	0.71
{311}	0.226	0.187	3.9313	4.32001	4.13023	0.45
{222}	0.138	0.062	2.36405	3.52313	3.0001	0.43

3.3. Microstructure analysis by TEM

TEM investigation of the microstructure of Cu-Zr thin films was detailed in the earlier study by Oellers et al. [24]. Following are the major microstructural observations from the STEM images of the Cu-

Zr thin films (Fig. 5 and 6): (i) For all Zr compositions, cross-sectional STEM micrographs exhibited columnar grains (Fig. 5(a)-(c)); (ii) average crystallites/grains size decreased with increasing Zr content; (iii) pores/voids are aligned along the columnar grain boundaries and such porosity decreased with increasing Zr content

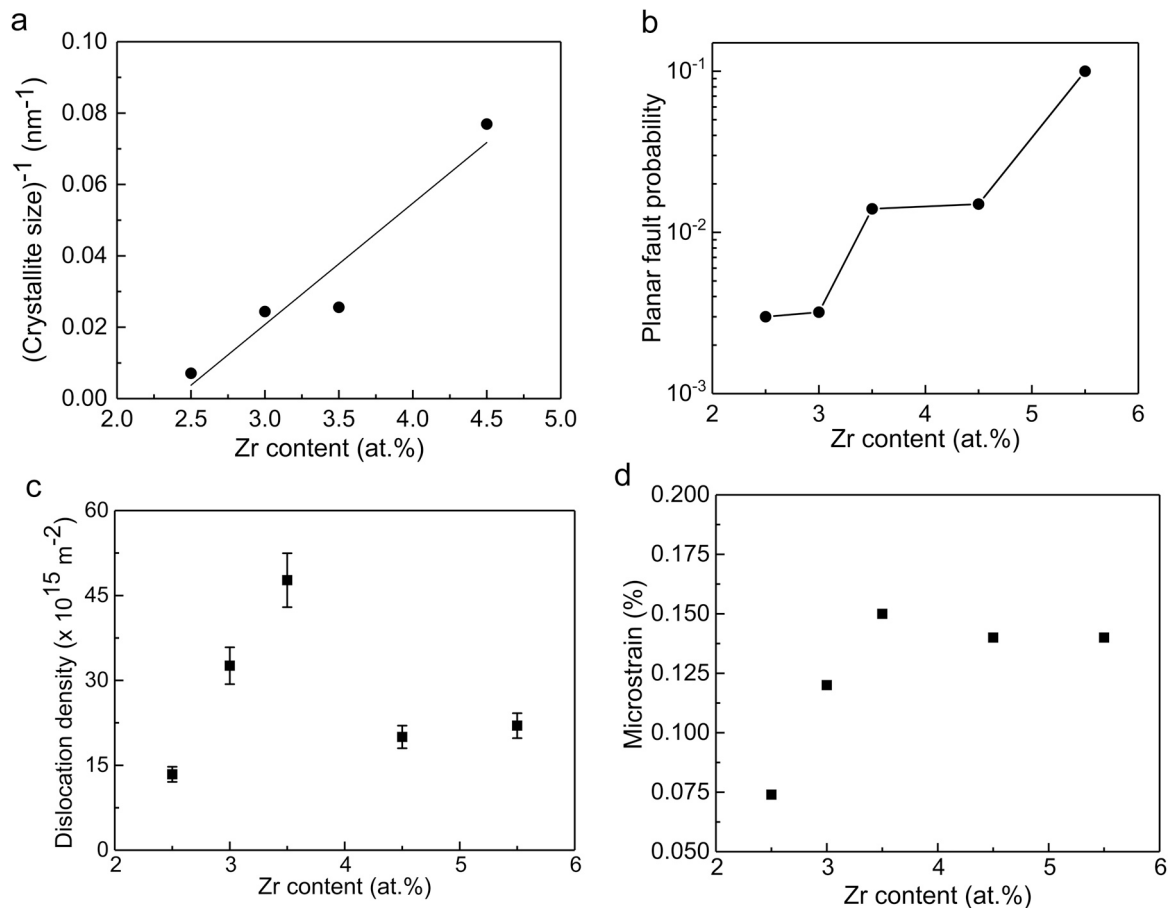


Fig. 4. (a) Average crystallite sizes of Cu-Zr alloy thin films plotted as a function of Zr composition. Inset graph shows plot of inverse crystallite size with Zr composition (a linear variation is obtained up to 4.5 at% Zr). Crystallite sizes were taken from Oellers et al. [24]; (b) Probability of planar faults plotted as a function of Zr composition in Cu-Zr thin films; (c) Dislocation density of the Cu-Zr alloy thin films plotted as a function of Zr composition; (d) Variation of microstrain with Zr composition in the Cu-Zr thin films.

Table 4

Crystallite size, dislocation type and average dislocation density from Modified W-H plots. Coefficient of determination (COD) or R² values for 'Modified-Williamson-Hall' plots are presented in the last column.

Zr composition (at%)	Size (nm)	Dislocation type	Average dislocation density (m ⁻²)	COD (R ²)
2.5	141	95% screw + 5% edge	13.4 × 10 ¹⁵	0.99
3.0	41	90% screw + 10% edge	32.6 × 10 ¹⁵	0.99
3.5	39	88% screw + 12% edge	47.7 × 10 ¹⁵	0.99
4.5	13	50% screw + 50% edge	20 × 10 ¹⁵	0.99
5.5	38	50% screw + 50% edge	22 × 10 ¹⁵	0.99

(Fig. 5(a)–(c)); (iv) dispersion of 5–30 nm sized crystallites are observed within the columnar grains; (v) STEM-EDS results indicated absence of Zr segregation at the grain boundaries ([24]) and absence of precipitates both inside the grains and at the grain boundaries; (vi) STEM images exhibited stacking faults/nano-twin boundaries in Cu-Zr thin films with 2.5, 4.5 & 5.5 at% Zr (Fig. 6(a)–(c)).

3.4. Residual stress analysis using traditional XRD and GIXRD methods

XRD stress analysis by traditional $d_{\psi}^{hkl} - \sin^2 \psi$ method indicated tensile stresses in the Cu-Zr thin films increasing monotonically with Zr composition (Fig. 7(a)). Fig. 7(b) shows that increasing Zr content led to a systematic increase in the curvature of the $d_{\psi}^{hkl} - \sin^2 \psi$ plots of the Cu-Zr thin films. In fact, stress analysis using the traditional XECs was not possible for the 5.5 at% Zr film because of considerable curvature in the observed $d_{\psi}^{hkl} - \sin^2 \psi$ plot. In general, such

non-linear $d_{\psi}^{hkl} - \sin^2 \psi$ plots are observed due to the crystallographic texture in the polycrystalline thin films [45,75]. However, the so-called 'direction dependent grain interaction' was also attributed to the observed non-linearity in the $d_{\psi}^{hkl} - \sin^2 \psi$ plots even in the absence of crystallographic texture in polycrystalline thin films [47,75–76]. Furthermore, non-linear $d_{\psi}^{hkl} - \sin^2 \psi$ plots may be due to the lattice strain gradient across the thickness of the Cu-Zr thin films (variation of tilt angle ' ψ ' changes the penetration depth of X-ray inside the thin film) [45]. In the present case, the Cu-Zr thin films have columnar grains predominantly oriented along the film surface normal and they exhibited both strong and sharp {111} fiber texture up to 3.5 at% Zr composition. Thus, the macroscopic elastic properties of the grains are rotationally symmetric with respect to the film surface normal (i.e. transversely isotropic). However, beyond 3.5 at% Zr, both strength and sharpness of {111} fiber texture drastically reduced along with almost random orientations of the crystallites for 5.5 at% Zr thin film (see Fig. 7(c)). Surprisingly, significant curvature in the $d_{\psi}^{hkl} - \sin^2 \psi$ plots also occurred only beyond 3.5 at% Zr composition. Therefore, the reason for the observed non-linear $d_{\psi}^{hkl} - \sin^2 \psi$ plots beyond 3.5 at% Zr may be either due to the direction dependent grain interaction or the lattice strain gradient across the thickness of these thin films. Since a detailed modeling of film stress using the direction dependent elastic grain interaction was beyond the scope of the present study, the possibility of stress gradients in the Cu-Zr thin films was examined by lattice strain measurements using the GIXRD geometry (Section 2.2 provides the detailed methodology). The presence of stress gradients in thin films and thin surface layers of materials was addressed by several researchers [47,49]. Diffraction stress analysis was performed using

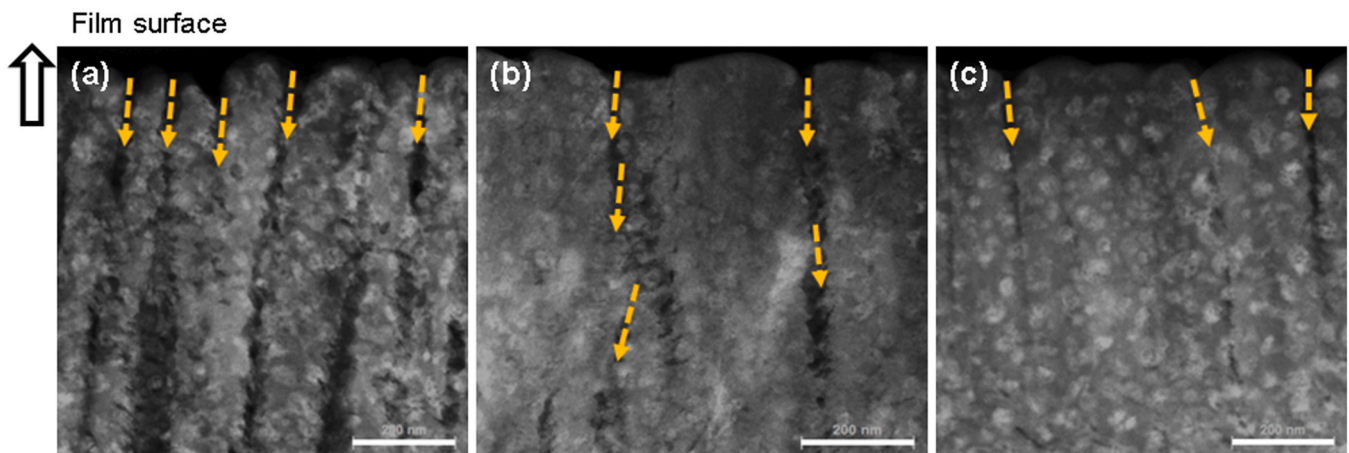


Fig. 5. STEM image (HAADF) of Cu-Zr thin film sections with different Zr compositions (a) 2.5 at% Zr ; (b) 4.5 at% Zr ; (c) 5.5 at% Zr. Grain boundary porosity channels are indicated by downward arrows placed adjacent to the channels. STEM image for 2.5 at% Zr is taken from [24] for comparison.

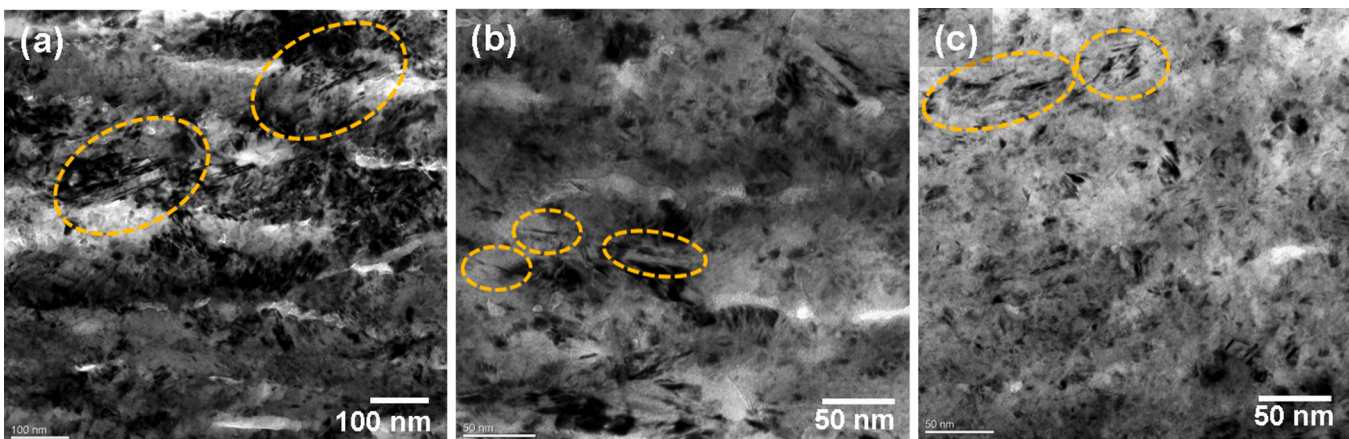


Fig. 6. STEM bright field (BF) images of the cross-sections of Cu-Zr thin films (close to the film surface) (a) 2.5 at% Zr, (b) 4.5 at% Zr; (c) 5.5 at% Zr. The planar faults are encircled in each of the micrographs.

the so-called $f(\psi, hkl)$ method [47] (see Section 2.2). Fig. 8(a)–(c) show the $\varepsilon_{\psi}^{hkl} - f(\psi, hkl)$ plots for all Zr compositions obtained from the measurements of lattice strains (ε_{ψ}^{hkl}) for various $\{hkl\}$ diffracting planes in the GIXRD geometry corresponding to three different incidence angles of X-ray (i.e. $\alpha = 1^\circ, 2^\circ, 3^\circ$). The approximate penetration depths of (τ) of X-ray ($\tau \sim \text{Sin}\alpha/\mu$; where μ is the linear absorption coefficient of Cu for $\text{CoK}\alpha$ X-ray radiation $\sim 731 \text{ cm}^{-1}$ [52]) are 0.25 μm , 0.5 μm and 0.75 μm for $\alpha = 1^\circ, 2^\circ$ and 3° respectively. No significant curvature was observed in the $\varepsilon_{\psi}^{hkl} - f(\psi, hkl)$ plots except for Zr composition ≥ 4.5 at% (Fig. 8(a)–(c)).

Straight lines fitted to the $\varepsilon_{\psi}^{hkl} - f(\psi, hkl)$ plots showed positive slopes for all Zr compositions. A positive slope indicates tensile stress distribution across the thickness of the Cu-Zr thin films (see Fig. 8(a)–(c)). However, it is important to note that for any particular Zr composition, the slope of straight line changes with angle of incidence of X-ray and hence across the film thickness which in turn implies a change of lattice strain gradient(s) across the film thickness. Fig. 9 shows the variation of these tensile stresses in the Cu-Zr thin films as a function of Zr composition for $\alpha = 1^\circ, 2^\circ$ and 3° . It is clear that up to 3 at% Zr the stresses in Cu-Zr films ranged between 50 MPa $\leq \sigma \leq$ 250 MPa with the change of X-ray incidence angle. For Cu-Zr thin films with Zr composition ≥ 3.5 at%, tensile stresses near the surface up to $\sim 0.25 \mu\text{m}$ were much higher than those observed below ($> 0.25 \mu\text{m}$).

4. Discussion

4.1. Zr alloying of Cu in Cu-Zr thin films

The above experimental results indicated formation of a substitutional solid solution between Cu and Zr in the as-deposited Cu-Zr thin films for Zr contents ranging from 2.5–5.5 at%. The alloying between Cu and Zr was confirmed from the linear increase of strain free lattice parameters of the Cu-Zr thin films up to 4.5 at% Zr. Furthermore, neither GIXRD nor STEM-EDS showed Zr segregation and/or formation of Cu-Zr amorphous phases at the Cu grain boundaries in the room temperature deposited Cu-Zr thin films for the investigated Zr compositions [24]. From kinetic viewpoint, direct deposition of Cu and Zr from the vapor phase and quenching the vapors on the cold/unheated substrate at room temperature leads to non-equilibrium Cu-Zr alloy films since bulk (volume) diffusion of Zr atoms through the Cu lattice is a sluggish process. In recent years such non-equilibrium techniques were exploited to achieve almost 100% solid solubility between elements with a large positive enthalpy of mixing such as the Cu-Cr system ($\Delta H^{\text{mix}} \sim 20 \text{ kJ/mole}$) [77,78].

The Cu-Zr solid solubility observed in the present work is in contrast with recent observations of amorphous phase at the Cu grain boundaries in similar Cu-Zr thin films with ≥ 2 at% Zr [16,21]. In

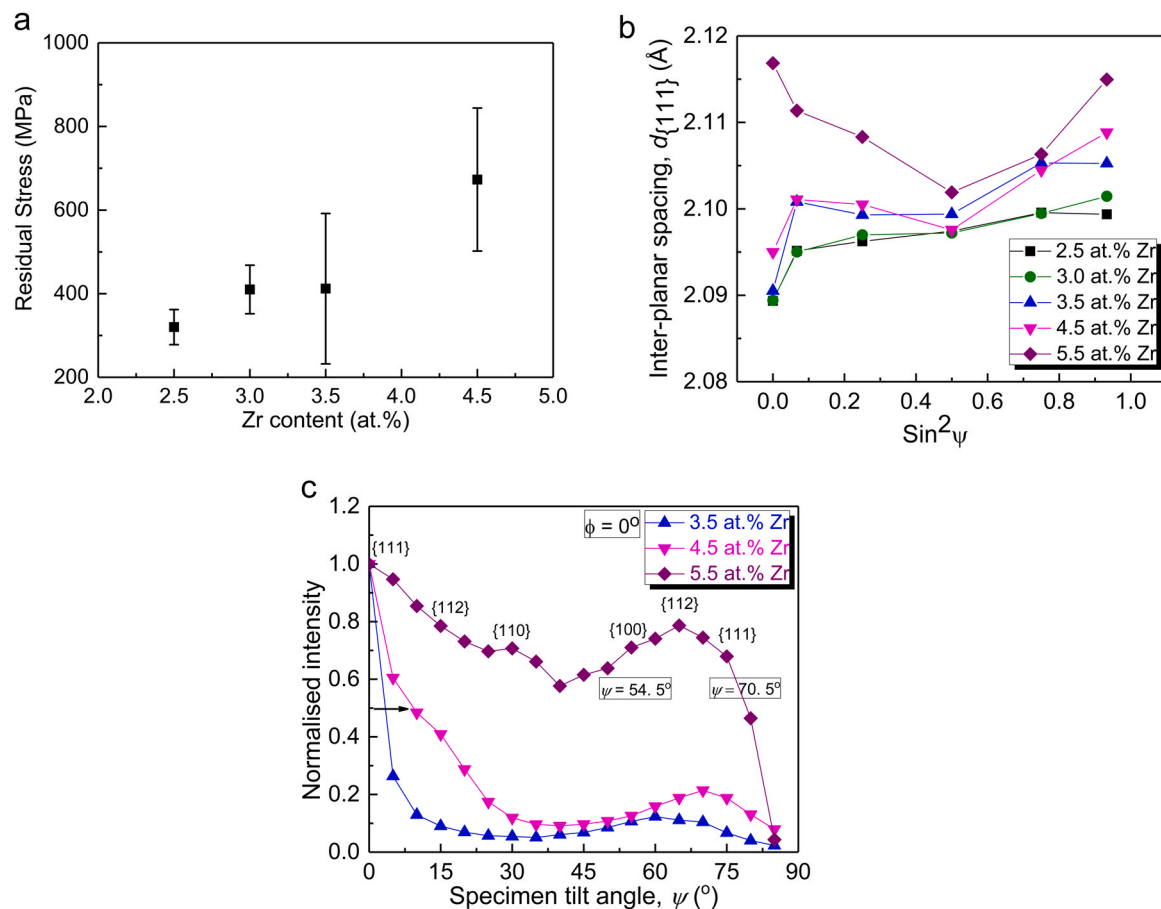


Fig. 7. (a) Stress change with Zr composition – diffraction stress analysis using traditional $d - \sin^2\psi$ method; (b) $d - \sin^2\psi$ plots replotted from [24]; (c) Fiber plots of Cu-Zr thin films for different Zr compositions - Normalized intensity plotted as a function of specimen tilt angle (ψ) (for fixed specimen rotation angle, $\phi = 0^\circ$) (data replotted from [24]).

addition, these authors reported the grain boundary segregation of Zr atoms in Cu-Zr thin films at lower Zr content (~ up to 1 at%) [16,21]. Thermodynamically, such segregation of Zr atoms and/or formation of amorphous phase leads to significant reduction of grain boundary energy in nanostructured Cu-Zr thin films [11–13,16]. Furthermore, due to large atomic size mismatch between Cu and Zr atoms, Zr segregation can significantly reduce the elastic strain energy of the Cu-Zr thin films by transferring the Zr atoms from lattice sites to grain boundary sites. Since, both phenomena are absent in the present case, the Cu-Zr thin films possess excess grain boundary energy and increased elastic strain energy due to the lattice defects and intrinsic stresses. Hence, the enhanced solid solubility between Cu and Zr atoms up to 5.5 at% Zr results from room temperature grain boundary diffusion combined with lateral volume diffusion of Zr atoms in the Cu matrix. The generation of high density of lattice defects in the Cu lattice due to Zr incorporation and also otherwise may lead to reduction of activation energy of volume diffusion of Zr atoms in Cu matrix. In particular, high dislocation density and planar faults in the Cu-Zr thin films were confirmed from the XLPAs investigation (see Section 3.2). These dislocations can act as short circuit paths for the diffusion of Zr atoms into Cu lattice even at room temperature extending the Cu-Zr solid solubility beyond the equilibrium limit. Thermodynamically, dislocation stress field can alter the chemical potential of the Zr solute atoms present in the immediate vicinity of the dislocations which may result in a change of Zr concentration and therefore a change of solubility [79,80]. However, a rough estimate of enhanced Zr concentration due to tensile stresses in the films indicates only a factor of four increase as compared to the room temperature solid solubility of Zr in Cu (~ 0.015 at% [14]) which cannot account for the observed solubility of

2.5–5.5 at% Zr in Cu. Enhanced Zr solubility is possible by reducing the distance of the Zr solute atom from the core of an edge dislocation which could be achieved in presence of stacking faults (i.e. Suzuki effect [81,82]). It is possible that at Zr composition > 3.5 at%, dislocation splitting generates two Shockley partials connected by a stacking fault ribbon between them (see next section for details) and equilibrium concentration of Zr atoms within such faulted region can be significantly different from the average concentration in the rest of the Cu lattice [81,82].

4.2. Evolution of microstructure, texture and stress on Zr alloying

Zr alloying resulted in the following changes in the microstructure, texture and stress in the polycrystalline Cu-Zr thin films: (i) dislocations and planar faults generation resulting microstrain; (ii) grain refinement/nanostructuring of Cu matrix along with change of crystallographic texture; (iii) tensile stress generation and stress gradient across the film thickness.

4.2.1. Dislocations and planar faults generation

XLPAs of all polycrystalline Cu-Zr thin films showed large dislocation densities $\sim 10^{16}/\text{m}^2$ in the room temperature deposited state. The dislocations caused anisotropic strain broadening of the XRD line profiles and large inhomogeneous lattice strains ($\epsilon \geq 0.2\%$ for 4.5 at% Zr) in the Cu-Zr thin films. Dislocations are generated in order to accommodate large amount of lattice strains in the thin films originated from: (i) macroscopic films stresses due to non-equilibrium growth of the thin films and subsequent atomic rearrangement on the substrate; (ii) compositional lattice strains due to large atomic size misfit between Cu and Zr atoms; (iii) formation

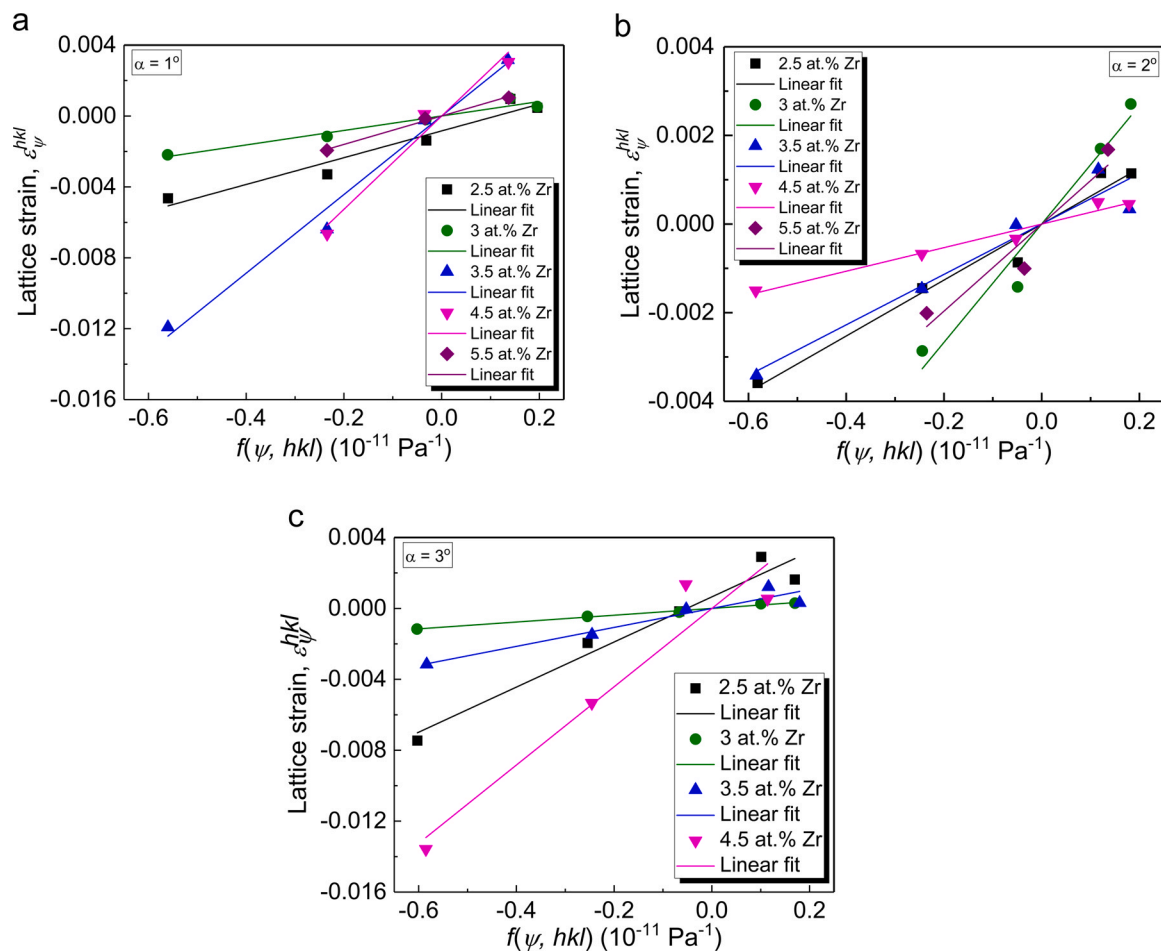


Fig. 8. Lattice strains ϵ_{ψ}^{hkl} plotted as a function of $f(\psi, hkl)$ obtained from the GIXRD stress measurements at incidence angle of (a) 1° , (b) 2° and (c) 3° of the Cu-Zr thin films. Due to curvature of the plots for ≥ 4.5 at% Zr some data points are omitted for certain incident angles.

of sub-grain boundaries. Additional dislocation generation may be due to the formation of pairs of Zr-Zr near-neighbor bonds during the movement of a single dislocation [39,41]. Since Zr atoms repel each other, Zr-Zr bond formation increases the local free energy leading to the generation of additional ‘chemically necessary’ dislocations. [39,41].

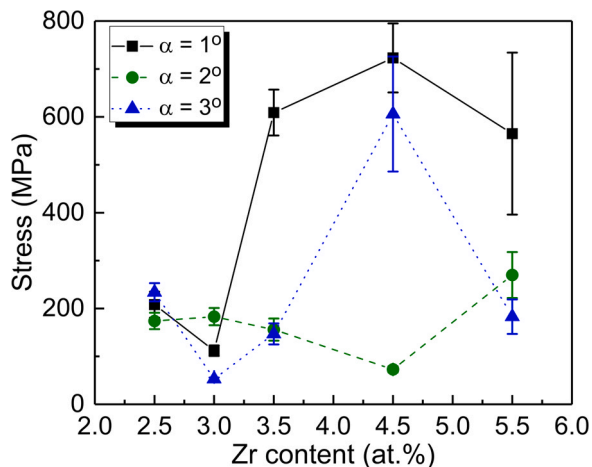


Fig. 9. Variation of stress as a function of Zr composition for various incident angles obtained using the GIXRD stress measurements.

The XLPDA deduced dislocations in Cu-Zr thin films have predominantly screw character at relatively low ≤ 3.5 at% Zr and mixed character for Zr content ≥ 3.5 at%. The decrease in the screw dislocation fraction may be due to the dissociation of individual perfect screw dislocation into two Shockley partial dislocations (SPDs) (i.e. formation of an extended dislocation: $\frac{a}{2}[10\bar{1}] = \frac{a}{6}[11\bar{2}] + \frac{a}{6}[2\bar{1}\bar{1}] + \text{stacking fault}$) in fcc Cu-Zr alloy and/or dislocation annihilation by the recombination of the two partial dislocations and cross slip [81,83].

Dislocation microstructure of severely plastically deformed ultrafine grained Cu evaluated by the XLPDA also exhibited a similar decrease of screw dislocation fraction by dislocation annihilation/recovery by the cross slip of screw dislocations [72]. However, recovery of dislocations by the recombination of dissociated dislocations and cross slip seems to be difficult due to an anticipated decrease of SFE of the Cu matrix with increasing Zr content. Lowering of SFE due to Zr addition to the dilute Cu-1 wt%Cr alloy was reported earlier in the literature [34]. The addition of Zn also reduced the SFE of Cu along with an increase of planar fault probability in a plastically deformed Cu-Zn alloy [33,35]. Similarly, addition of Al reduced the SFE in the Cu-Al alloy [39]. However, neither theoretical calculation nor experimental evidence of SFE reduction of Cu due to Zr addition was found in the literature particularly for the Zr composition investigated in the present work.

SFE reduction leads to easier dissociation of perfect screw dislocation and formation of a stacking fault ribbon between the two SPDs especially at ≥ 3.5 at% Zr. Additionally, from a thermodynamic

viewpoint, dislocation dissociation leads to the reduction of total elastic strain energy of the Cu-Zr thin films since the energy per unit length of a perfect screw dislocation is $\frac{1}{2}Gb^2$ whereas the energy per unit length of a partial dislocation is $\frac{1}{3}(\frac{1}{2}Gb^2)$. Presence of these stacking faults in the Cu-Zr thin films was indicated by the lattice parameter anisotropy observed for all Zr compositions (Section 3.1). Additionally, XLPAs showed an overall increase of planar fault (stacking faults and/or twin faults) probability (≤ 0.1) with increasing Zr content.

Lowering of SFE may also facilitate twin formation in Cu matrix. Zhang et al. observed twin boundaries in magnetron sputtered Cu-Zr thin films on Zr addition [16,21]. Twin faults in the fcc Cu matrix are known to cause asymmetry of the Cu diffraction peaks [52]. However, significant overlapping between the Cu diffraction peaks and broadening prevented unambiguous detection of twin faults from the GIXRD patterns of the Cu-Zr thin films. However, cross-sectional TEM confirmed the presence of a few twin faults (and stacking faults) in the microstructure of Cu-Zr thin films (Fig. 6). Finally, it must be mentioned that the presence of dislocations and planar faults in the microstructure of Cu-Zr thin films play key roles in the grain refinement, texture development (see next section) and enhanced solid solubility of Zr in Cu. These in turn improve the mechanical properties of the Cu-Zr thin films such as increased hardness of the thin films [24].

4.2.2. Grain refinement and texture development

Both XRD and TEM results indicated that the Zr atoms act as grain refiner for the polycrystalline Cu-Zr thin films. Nanometer sized crystallites/grains (lowest average crystallite size ~ 13 nm) were observed within the columnar grains of the thin films with ≥ 4.5 at% Zr. These nanocrystallites were not the Cu-Zr intermetallic phase(s) known from the Cu-Zr equilibrium phase diagram [14,15] since the GIXRD patterns did not show any Bragg peaks corresponding to any of these phases. Grain refinement was accompanied by the decrease of both strength and sharpness of {111} fiber texture with increasing Zr content (Fig. 7(c)) indicating that the Zr also acts as texture weakening agent. Randomly oriented nanometer sized crystallites (≤ 25 nm) can be observed throughout the columnar grains (Fig. 5(c)).

Grain refinement in magnetron sputtered polycrystalline Cu-Zr thin films [16,21] was explained on the basis of the real structure zone model (RSZM) [84,85] of alloy thin film deposition. According to the RSZM model, the grain refinement occurs due to the segregation of the solute atoms/alloying elements at the grain boundaries or on the surfaces of individual islands. These processes not only inhibit the grain growth but also weaken the crystallographic texture due to reduced grain boundary migration both at the coalescence and grain coarsening stages [84,85]. However, both XRD and STEM-EDS results [24] indicated that the Zr atoms impinging on the film surface are dissolved in the Cu lattice as substitutional solutes. Therefore, the grain refinement observed in Cu-Zr thin films cannot be understood from the grain boundary segregation of Zr atoms using RSZM.

In the present case, the kinetics of grain refinement and texture development during the deposition of Cu-Zr thin films may be governed by (i) nucleation and growth rate of crystallites at room temperature; (ii) generation and motion of dislocations, extended dislocations and planar faults with increasing Zr composition; (iii) solute drag effect: interaction of dislocations and grain boundaries with Zr solute atoms predominantly at higher Zr composition which limits dislocation motion and final crystallite/grain size.

(i) growth rate of crystallites is strongly dependent on the mobility of Zr atoms in Cu lattice during room temperature deposition of Cu-Zr thin films [86]. At low Zr composition, crystallite growth is predominantly controlled by surface and grain boundary diffusion of Zr atoms whereas at higher Zr composition, crystallite growth requires long range volume diffusion. Since, the

volume diffusion coefficient of Zr atoms in the Cu lattice is small at room temperature, the crystallite growth rate may be retarded with increasing Zr composition.

- (ii) XLPAs indicated the generation of dislocations and planar faults due to Zr addition during the deposition of Cu-Zr thin films. These dislocations can move on the {111} slip planes if the film stress is higher than the yield strength of the Cu-Zr thin films. Theoretical calculation of film stresses (not presented here) revealed that the stresses generated due to various microstructural changes during the deposition of the Cu-Zr thin films can be much higher than the typical yield strength of 2 μm thick polycrystalline Cu thin film on Si(100) substrate (~ 500 MPa [1,16,21]). Furthermore, XRD stress analysis by $d_{\psi}^{hkl} - \sin^2\psi$ method indicated residual stresses ≥ 500 MPa in the Cu-Zr thin films with > 3 at% Zr. However, plastic deformation mechanism and generation of planar faults depends strongly on the SFE of the Cu-Zr thin films which is expected to decrease due to Zr addition particularly beyond 3 at% Zr. Therefore, both the grain refinement and plastic deformation mechanisms of Cu-Zr thin films strongly depend on the Zr content. At relatively low Zr composition up to 3 at% Zr with low planar fault probability (β) ~ 0.003 , it is plausible that the mechanism of grain refinement is predominantly governed by the motion of screw dislocations (maximum $\rho \sim 3 \times 10^{16}/\text{m}^2$). During initial stage of grain refinement, movement of dislocations through the coarse columnar grains may generate dislocation walls/cell walls with small misorientation angles. These cell walls may eventually form subgrain boundaries with gradual increase of dislocation density dividing the original coarse grain into smaller ~ 45 nm grains along with the formation of high angle boundaries. In this context it may be noted that the XLPAs is sensitive to dislocation cells with small misorientation angles of $1-2^\circ$ [73] whereas these cells can only be discerned by high resolution TEM. This is why the average crystallite size measured by XLPAs is often smaller than the average grain size measured by TEM. At Zr composition ≥ 3.5 at%, large number of stacking faults and twins are generated ($\beta \geq 1\%$ from Fig. 4(b)) due to the significant decrease of SFE of the Cu matrix. These faults can restrict the movement of dislocations and facilitate grain refinement by the formation of deformation twins [39,41]. Stacking faults and twins produce boundaries inside the columnar grains contributing to size broadening in the XLPAs by decreasing the effective size of the coherently diffracting domains [53,73]. Similar grain refinement mechanisms were reported in severely plastically deformed Cu-Al and Cu-Zn alloys due to reduction of SFE of Cu [2,38,39].
- (iii) Finally, the grain refinement mechanisms via dislocation motion and planar faults saturate when Zr solute atoms start interacting with the dislocations and grain boundaries setting the lower limit of the crystallite size. Dislocation motion is retarded and/or locked due to the Zr solute atoms leading to solid solution hardening of the Cu-Zr thin films [24].

Such dislocation locking mechanisms were confirmed by the approximately linear dependence of the inverse crystallite size ($1/d$) on the Zr composition (Fig. 4(a) inset graph). Dislocations may be either elastically locked due to Cu-Zr atomic size mismatch or chemically locked by the Zr atoms segregated at the stacking faults in the fcc Cu-Zr lattice [80,87–88]. Both of these locking processes may occur since atomic size mismatch between Cu and Zr atoms is high $\sim 24\%$ and Cu-Zr thin films exhibit large planar fault probability resulting in a steady state value of the crystallite/grain size.

4.2.3. Stress and stress gradient evolution

Possible origins of tensile stresses in the Cu-Zr thin films and their variation along the film thickness direction (up to ~ 0.75 μm)

and for different Zr content are discussed next. Firstly, it is noteworthy that the tensile stresses obtained using the $d_{\psi}^{hkl} - \sin^2 \psi$ method refers to the average stress over the entire cross-section up to 2 μm film thickness whereas the GIXRD stress measurement method probes the tensile stress gradient up to maximum depth of 0.75 μm below the film surface for a fixed Zr content (Fig. 9).

During the room temperature deposition of a co-sputtered Cu-Zr thin film, Cu atoms and Zr atoms arrive at the substrate more rapidly than they rearrange on the substrate forming a non-equilibrium microstructure. The rearrangement on the substrate occurs by diffusion of the atomic species. Due to low diffusivities of Cu and Zr atoms at the substrate/room temperature, limited rearrangement and columnar growth is expected [86]. Therefore, microstructure of the Cu-Zr thin film consists of columnar grains having non-equilibrium grain boundaries with voids/pores in the grain boundary channel and a large density of lattice defects such as excess vacancies, dislocations and planar faults inside the grains. Subsequently, gradual relaxation of the grain boundaries and progressive shrinkage of the columnar grain boundary voids occur due to the increase in nucleation rate with respect to grain growth with increasing Zr content. As a consequence, diffusion along the grain boundaries becomes more prominent which leads to gradual densification of the films. Densification generates tensile stress in the thin film [89] due to the constraint of the rigid substrate. Interestingly, tensile stresses increased monotonically up to 4.5 at% Zr (Fig. 7(a)) along with reduction in grain boundary porosity with increasing Zr composition (Fig. 5(a)–(c)). Furthermore, the tensile stresses at the film surface up to $\sim 0.25 \mu\text{m}$ are different than those observed in the subsurface region ($0.25 \mu\text{m} \leq \text{depth} \leq 0.75 \mu\text{m}$) particularly in films having ≥ 3.5 at% Zr (Fig. 9). Qualitatively, this indicates significant variation of microstructure (i.e. porosity, grain size/size distribution, and defect density) and possibly crystallographic texture along the thickness direction especially for thin films with Zr composition ≥ 3.5 at% assuming Zr composition is homogeneous across the depth for all Cu-Zr thin films. Thin films having Zr composition ≤ 3 at% exhibited porous microstructure continuously from the film surface up to the depth of 0.75 μm (Fig. 5(a)) and as a consequence relatively low tensile stresses without much stress gradient (up to 0.75 μm depth) was observed (Fig. 9). However, the average stresses obtained from the $d_{\psi}^{hkl} - \sin^2 \psi$ method (Fig. 7(a)) for the thin films having ≤ 3 at% Zr are considerably higher than those observed from the GIXRD stress analysis (Fig. 9). The reason for this observed difference may be higher film stresses close to the substrate which not probed by GIXRD due to the small incidence angles. However, it is noteworthy that any possible relaxation of tensile stress by dislocation motion was neglected in the above discussion as expected to be negligible for small grain sizes [90,91].

5. Conclusions

The major conclusions derived from the present investigation of the effects of Zr content on the microstructure evolution and residual stress development in nanostructured room temperature deposited $\text{Cu}_{100-x}\text{-Zr}_x$ thin films are as follows:

1. GIXRD phase analysis, strain free lattice parameters and the STEM-EDS confirmed the formation of non-equilibrium $\text{Cu}_{100-x}\text{-Zr}_x$ solid solutions with 2.5 at% $\leq x \leq 5.5$ at% Zr without Zr segregation and amorphous phase formation at the Cu grain boundaries.
2. Grain refinement and texture weakening occurred in the Cu-Zr thin films with increasing Zr content: almost random orientation of crystallites was obtained at 5.5 at% Zr.
3. The XLPD confirmed large dislocation density and finite probability (≤ 0.1) of planar faults (both stacking faults and twins) in thin films

due to Zr addition. The generation of stacking faults was also supported by the observed lattice parameter anisotropy in Cu-Zr thin films. Such planar faults generation was attributed to the reduction in stacking fault energy of Cu due to addition of Zr solutes.

4. The traditional $d_{\psi}^{hkl} - \sin^2 \psi$ stress analysis method confirmed generation of tensile stresses monotonically increasing with Zr composition in the Cu-Zr thin films. GIXRD stress measurements revealed considerable tensile stress gradients in the Cu-Zr thin films especially at ≥ 3.5 at% Zr possibly due to increasing microstructural gradients across the film thickness at ≥ 3.5 at% Zr.

CRedit authorship contribution statement

J. Chakraborty: XRD experiments, XLPD and stress analysis, data interpretation and preparation of original draft of the manuscript. **T. Oellers:** Thin film deposition, chemical composition analysis, film thickness measurement and TEM experiments and data analysis. **R. Raghavan:** Thin film deposition, analysis of microstructure from TEM data, assistance in preparing the original and the revised version of the manuscript including preparation of figures. **G. Dehm:** Research problem conceptualization, funding acquisition; facilitating all experiments, correction of original draft of the manuscript and overall guidance. **A. Ludwig:** Research problem conceptualization, overall supervision of the work and manuscript correction for final submission.

Declaration of Competing Interest

The authors declare that they have no known competing financial interests or personal relationships that could have appeared to influence the work reported in this paper. Therefore, no potential conflict of interest was reported by the author(s).

Acknowledgements

The authors would like to thank Mr. Benjamin Breitbach for assistance in conducting the XRD experiments and analysis. T. Oellers acknowledges a Ph.D fellowship from the International Max Planck Research School for Surface and Interface Engineering (IMPRS-SurMat). GD acknowledges financial support by the ERC Advanced Grant GB-CORRELATE (grant number 787446).

Disclosure statement

No potential conflict of interest was reported by the author(s).

Appendix A. Supporting information

Supplementary data associated with this article can be found in the online version at doi:10.1016/j.jallcom.2021.162799.

References

- [1] J. Schiøtz, K.W. Jacobsen, A maximum in the strength of nanocrystalline copper, *Science* 301 (2003) 1357–1359, <https://doi.org/10.1126/science.1086636>
- [2] T.G. Langdon, Twenty-five years of ultrafine-grained materials: achieving exceptional properties through grain refinement, *Acta Mater.* 61 (2013) 7035–7059, <https://doi.org/10.1016/j.actamat.2013.08.018>
- [3] K.M. Youssef, R.O. Scattergood, K.L. Murty, J.A. Horton, C.C. Koch, Ultrahigh strength and high ductility in bulk nanocrystalline copper, *Appl. Phys. Lett.* 87 (2005), <https://doi.org/10.1063/1.2034122> (091904-1-3).
- [4] L. Lu, N.R. Tao, L.R. Tao, L.R. Wang, R.Z. Ding, K. Lu, Grain growth and strain release in nanocrystalline copper, *J. Appl. Phys.* 89 (2001), <https://doi.org/10.1063/1.1367401> (3414–3408).
- [5] V.Y. Gertsman, R. Birringer, On the room temperature grain growth of nanocrystalline copper, *Scr. Met. Mater.* 30 (1994) 577–581, [https://doi.org/10.1016/0956-716X\(94\)90432-4](https://doi.org/10.1016/0956-716X(94)90432-4)
- [6] M. Ames, J. Markmann, R. Karos, A. Michels, A. Tschöpe, R. Birringer, Unraveling the nature of room temperature grain growth in nanocrystalline materials, *Acta Mater.* 56 (2008) 4255–4266, <https://doi.org/10.1016/j.actamat.2008.04.051>

- [7] H.A. Murdoch, C.A. Schuh, Stability of binary nanocrystalline alloys against grain growth and phase separation, *Acta Mater.* 61 (2013) 2121–2132, <https://doi.org/10.1016/j.actamat.2012.12.033>
- [8] J.R. Weertman, Retaining the nano in nanocrystalline alloys, *Science* 337 (2012) 921–922, <https://doi.org/10.1126/science.1226724>
- [9] T.J. Rupert, J.C. Trenkle, C.A. Schuh, Enhanced solid solution effects on the strength of nanocrystalline alloys, *Acta Mater.* 59 (2011) 1619–1631, <https://doi.org/10.1016/j.actamat.2010.11.026>
- [10] J. Weissmuller, Alloy effects in nanostructures, *Nanostruct. Mater.* 3 (1993) 261–272, [https://doi.org/10.1016/0965-9773\(93\)90088-S](https://doi.org/10.1016/0965-9773(93)90088-S)
- [11] M.A. Atwater, R.O. Scattergood, C.C. Koch, The stabilization of nanocrystalline copper by Zirconium, *Mater. Sci. Eng. A* 559 (2013) 250–256, <https://doi.org/10.1016/j.msea.2012.08.092>
- [12] M. Saber, H. Kotan, C.C. Koch, R.O. Scattergood, Thermodynamic stabilization of nanocrystalline binary alloys, *J. Appl. Phys.* 113 (2013), <https://doi.org/10.1063/1.4791704> (063515-1-11).
- [13] K.A. Darling, M.A. Tschopp, B.K. Vanleeuwen, M.A. Atwater, Z.K. Liu, Mitigating grain growth in binary nanocrystalline alloys through solute selection based on thermodynamic stability maps, *Comp. Mater. Sci.* 84 (2014) 255–266, <https://doi.org/10.1016/j.commatsci.2013.10.018>
- [14] D. Arias, J.P. Abriata, Copper-Zirconium phase diagram, *Bull. Alloy Phase Diagr.* 11 (1990) 452–459, <https://doi.org/10.31399/asm.hb.v03.a0006159>
- [15] N. Wang, C. Li, Z. Du, F. Wang, W. Zhang, The thermodynamic re-assessment of the Cu–Zr system, *CALPHAD* 30 (2006) 461–469, <https://doi.org/10.1016/j.calphad.2006.06.002>
- [16] P. Zhang, J.Y. Zhang, J. Li, G. Liu, K. Wu, Y.Q. Wang, J. Sun, Microstructural evolution, mechanical properties and deformation mechanisms of nanocrystalline Cu thin films alloyed with Zr, *Acta Mater.* 76 (2014) 221–237, <https://doi.org/10.1016/j.actamat.2014.04.041>
- [17] V.B. Borovikov, M.I. Mendeleev, A.H. King, Effects of Ag and Zr solutes on dislocation emission from the sigma11(332) [110] symmetric tilt grain boundary in Cu: bigger is not always better, *Int. J. Plast.* 109 (2018) 79–87, <https://doi.org/10.1016/j.jiplas.2018.05.009>
- [18] M. Azimi, G.H. Akbari, Development of nano-structure Cu–Zr alloys by the mechanical alloying process, *J. Alloy. Compd.* 509 (2011) 27–32, <https://doi.org/10.1016/j.jallcom.2010.08.071>
- [19] D. Roy, M.A. Atwater, K. Youssef, J.C. Ledford, R.O. Scattergood, C.C. Koch, Studies on thermal stability, mechanical and electrical properties of nano crystalline Cu_{99.5}Zr_{0.5} alloy, *J. Alloy. Compd.* 558 (2013) 44–49, <https://doi.org/10.1016/j.jallcom.2012.11.004>
- [20] Khalajhedayati, T.J. Rupert, High temperature stability and grain boundary complexion formation in a nanocrystalline Cu–Zr alloy, *J. Met.* 67 (2015) 2788–2801, <https://doi.org/10.1007/s11837-015-1644-9>
- [21] J.T. Zhao, J.Y. Zhang, L.F. Cao, Y.Q. Wang, P. Zhang, K. Wu, G. Liu, J. Sun, Zr alloying effect on the microstructure evolution and plastic deformation of nanostructured Cu thin films, *Acta Mater.* 132 (2017) 550–564, <https://doi.org/10.1016/j.actamat.2017.05.007>
- [22] T.P. Weihs, T.W. Barbee Jr., M.A. Wall, Hardness, ductility and thermal processing of Cu/Zr and Cu/Cu–Zr nanoscale multilayer foils, *Acta Mater.* 45 (1997) 2307–2315, [https://doi.org/10.1016/S1359-6454\(96\)00370-9](https://doi.org/10.1016/S1359-6454(96)00370-9)
- [23] J.Y. Zhang, G. Liu, S.Y. Lei, J.J. Niu, J. Sun, Transition from homogeneous-like to shear-band deformation in nanolayered crystalline Cu/amorphous Cu–Zr micropillars: Intrinsic vs. extrinsic size effect, *Acta Mater.* 60 (2012) 7183–7196, <https://doi.org/10.1016/j.actamat.2012.09.027>
- [24] T. Oellers, R. Raghavan, J. Chakraborty, C. Kirchlechner, A. Kostka, C.H. Liebscher, G. Dehm, A. Ludwig, Microstructure and mechanical properties in the thin film system Cu–Zr, *Thin Solid Films* 645 (2018) 193–202, <https://doi.org/10.1016/j.tsf.2017.10.030>
- [25] N. Muramatsu, H. Kimura, A. Inoue, Microstructures and mechanical properties of highly electrically conductive Cu_{0.5}, Cu₁ and Cu₂ at % Zr Alloy Wires, *Mater. Trans.* 54 (2013) 176–183, <https://doi.org/10.2320/matertrans.M2012264>
- [26] J. Wongsangam, M. Kawasaki, T.G. Langdon, The development of hardness homogeneity in a Cu–Zr alloy processed by equal-channel angular pressing, *Mater. Sci. Eng. A* 556 (2012) 526–532, <https://doi.org/10.1016/j.msea.2012.07.022>
- [27] J. Wongsangam, M. Kawasaki, T.G. Langdon, A comparison of microstructures and mechanical properties in a Cu–Zr alloy processed using different SPD techniques, *J. Mater. Sci.* 48 (2013) 4653–4660, <https://doi.org/10.1007/s10853-012-7072-0>
- [28] J. Wongsangam, H. Wen, T.G. Langdon, Microstructural evolution in a Cu–Zr alloy processed by a combination of ECAP and HPT, *Mater. Sci. Eng. A* 579 (2013) 126–135, <https://doi.org/10.1016/j.msea.2013.05.010>
- [29] R.B. Schwarz, Microscopic model for mechanical alloying, *Mater. Sci. Forum* 269–272 (1998) 665–674, <https://doi.org/10.4028/www.scientific.net/MSF.269-272.665>
- [30] E. Ma, M. Atzmon, F. Pinkerton, Thermodynamic and magnetic properties of metastable Fe₃Cu_{100-x} solid solutions formed by mechanical alloying, *J. Appl. Phys.* 74 (1993) 955–962, <https://doi.org/10.1063/1.354837>
- [31] A.G. Dirks, J.J. Van, Den broek, Metastable solid solutions in vapour deposited Cu–Cr, Cu–Mo and Cu–W thin films, *J. Vac. Sci. Technol. A* 3 (1985) 2618–2622, <https://doi.org/10.1116/1.572799>
- [32] C. Aguilar, V. de, P. Martinez, J.M. Palacios, S. Ordonez, O. Pavez, A thermodynamic approach to energy storage on mechanical alloying of Cu–Cr system, *Scr. Mater.* 57 (2007) 213–216, <https://doi.org/10.1016/j.scriptamat.2007.04.006>
- [33] K. Kapoor, D. Lahiri, I.S. Batra, S.V.R. Rao, T. Sanyal, X-ray Diffraction line profile analysis for defect study in Cu-1wt%Cr-0.1wt%Zr alloy, *J. Mater. Charact.* 54 (2005) 131–140, <https://doi.org/10.1016/j.jmchar.2004.09.009>
- [34] I.S. Batra, G.K. Dey, U.D. Kulkarni, S. Banerjee, Microstructure and properties of a Cu–Cr–Zr alloy, *J. Nucl. Mater.* 299 (2001) 91–100, [https://doi.org/10.1016/S0022-3115\(01\)00691-2](https://doi.org/10.1016/S0022-3115(01)00691-2)
- [35] C.N.J. Wagner, J.C. Helion, X-ray measurements of stacking faults and internal strains in α -Cu–Zn and α -Cu–Sn, *J. Appl. Phys.* 36 (1965) 2830–2837, <https://doi.org/10.1063/1.1714589>
- [36] I. Delehouze, A. Deruyttere, The stacking fault density in solid solutions based on copper, silver, nickel, aluminum and lead, *Acta Met* 15 (1967) 727–734, [https://doi.org/10.1016/0001-6160\(67\)90353-7](https://doi.org/10.1016/0001-6160(67)90353-7)
- [37] A. Howie, P.R. Swann, Direct measurement of stacking fault energies from observation of dislocation nodes, *Philos. Mag.* 6 (1961) 1215–1226, <https://doi.org/10.1080/14786436108243372>
- [38] Y.H. Zhao, X.Z. Liao, Y.T. Zhu, Z. Horita, T.G. Langdon, Influence of stacking fault energy on nanostructure formation under high pressure torsion, *Mater. Sci. Eng. A* 410–411 (2005) 188–193, <https://doi.org/10.1016/j.msea.2005.08.074>
- [39] S. Qu, X.H. An, H.J. Yang, C.X. Huang, G. Yang, Q.S. Zang, Z.G. Wang, S.D. Wu, Z.F. Zhang, Microstructural evolution and mechanical properties of Cu–Al alloys subjected to equal channel angular pressing, *Acta Mater.* 57 (2009) 1586–1601, <https://doi.org/10.1016/j.actamat.2008.12.002>
- [40] Y.Z. Tian, L.J. Zhao, S. Chen, A. Shibata, Z.F. Zhang, N. Tsuji, Significant contribution of stacking faults to the strain hardening behavior of Cu–15%Al alloy with different grain sizes, *Sci. Rep.* 5 (2015), <https://doi.org/10.1038/srep16707> (16707-1-9).
- [41] F.A. Mohamed, A dislocation model for the minimum grain size obtainable by milling, *Acta Mater.* 51 (2003) 4107–4119, [https://doi.org/10.1016/S1359-6454\(03\)00230-1](https://doi.org/10.1016/S1359-6454(03)00230-1)
- [42] M.J. Starink, X.G. Qiao, J. Zhang, N. Gao, Predicting grain refinement by cold severe plastic deformation in alloys using volume averaged dislocation generation, *Acta Mater.* 57 (2009) 5796–5811, <https://doi.org/10.1016/j.actamat.2009.08.006>
- [43] Y. Zhang, J. Guo, J. Chen, C. Wu, K.S. Kormout, P. Ghosh, Z. Zhang, On the stacking fault energy related deformation mechanism of nanocrystalline Cu and Cu alloys: A first principles and TEM study, *J. Alloy. Compd.* 776 (2019) 807–818, <https://doi.org/10.1016/j.jallcom.2018.12.075>
- [44] 'PROFIT', Profile fitting software, PANalytical, (formerly, Philips, Netherlands).
- [45] I.C. Noyan, J.B. Cohen, *Residual Stress*, Springer-Verlag New York Inc., 1987.
- [46] E.A. Brandes, G.B. Brook (Eds.), *Smithells Metals Reference Book*, 7th ed., Butterworth-Heinemann, 1998.
- [47] U. Welzel, J. Ligot, P. Lamparter, A.C. Vermeulen, E.J. Mittemeijer, Stress analysis of polycrystalline thin films and surface regions by X-ray diffraction, *J. Appl. Crystallogr.* 38 (2005) 1–29, <https://doi.org/10.1107/S0021889804029516>
- [48] J. Chakraborty, K. Kishor Kumar, S. Mukherjee, S.K. Ray, Stress, texture and microstructure of Zr thin films probed by X-ray diffraction, *Thin Solid Films* 516 (2008) 8479–8486, <https://doi.org/10.1016/j.tsf.2008.04.096>
- [49] K. Van Acker, L.D.E. Buysier, J.P. Celis, P. Van, Houtte, characterization of thin nickel electrocoatings by the low-angle diffraction method, *J. Appl. Cryst.* 27 (1994) 56–66, <https://doi.org/10.1107/S002188989300651X>
- [50] G.K. Williamson, W.H. Hall, X-ray line broadening from filed aluminium and Wolfram, *Acta Met.* 1 (1953) 22–31, [https://doi.org/10.1016/0001-6160\(53\)90006-6](https://doi.org/10.1016/0001-6160(53)90006-6)
- [51] T. Ungar, A. Borbely, The effect of dislocation contrast on X-ray line broadening: a new approach to line profile analysis, *Appl. Phys. Lett.* 69 (1996) 3173–3175, <https://doi.org/10.1063/1.117951>
- [52] B.E. Warren, *X-ray Diffraction*, Dover Publications INC., New York, 1969.
- [53] T. Ungar, S. Ott, P.G. Sanders, A. Borbely, J.R. Weertman, Dislocations, grain size and planar faults in nanostructured copper determined by high resolution X-ray diffraction and a new procedure of peak profile analysis, *Acta Mater.* 46 (1998) 3693–3699, [https://doi.org/10.1016/S1359-6454\(98\)00001-9](https://doi.org/10.1016/S1359-6454(98)00001-9)
- [54] T. Ungar, I. Dragomir, A. Revesz, A. Borbely, The contrast factors of dislocations in cubic crystals: the dislocation model of strain anisotropy in practice, *J. Appl. Cryst.* 32 (1999) 992–1002, <https://doi.org/10.1107/S0021889899009334>
- [55] T. Ungar, G. Tichy, The effect of dislocation contrast on X-ray line profiles in untextured polycrystals, *Phys. Stat. Sol.* 17 (1999) 42–43, [https://doi.org/10.1002/\(SICI\)1521-396X\(199902\)171:2<42::AID-PSSA425>3.0.CO;2-W](https://doi.org/10.1002/(SICI)1521-396X(199902)171:2<42::AID-PSSA425>3.0.CO;2-W)
- [56] E.J. Mittemeijer, P. Scardi (Eds.), *Diffraction Analysis of the Microstructure of Materials*, Springer, Germany, 2004.
- [57] S.N. Dey, P. Chatterjee, S.P. Sen Gupta, Dislocation induced line-broadening in cold-worked Pb–Bi binary alloy system in the α -phase using X-ray powder profile analysis, *Acta Mater.* 51 (2003) 4669–4677, [https://doi.org/10.1016/S1359-6454\(02\)00605-5](https://doi.org/10.1016/S1359-6454(02)00605-5)
- [58] R. Kuzel, Kinematical diffraction by distorted crystals-dislocation X-ray line broadening, *Z. Krist.* 222 (2007) 136–139, <https://doi.org/10.1524/zkri.2007.222.3-4.136>
- [59] E.J. Mittemeijer, U. Welzel, The 'state of the art' of the diffraction analysis of crystallite size and lattice strain, *Z. Krist.* 223 (2008) 552–560, <https://doi.org/10.1524/zkri.2008.1213>
- [60] A. Borbely, J. Dragomir-Cernatescu, G. Ribarik, T. Ungar, Computer program ANIZC for the calculation of diffraction contrast factors of dislocations in elastically anisotropic cubic, hexagonal and trigonal crystals, *J. Appl. Crystallogr.* 36 (2003) 160–162, <https://doi.org/10.1107/S0021889802021581>
- [61] M. Wilkens, The determination of density and distribution of dislocations in deformed single crystals from broadened X-ray diffraction profiles, *Phys. Stat. Sol.* A 2 (1970) 359–370, <https://doi.org/10.1002/pssa.19700020224>

- [62] A. Revesz, T. Ungar, A. Borbely, J. Lendvai, Dislocations and grain size in ball milled iron powder, *Nanostruct. Mater.* 7 (1996) 779–788, [https://doi.org/10.1016/S0965-9773\(96\)00048-7](https://doi.org/10.1016/S0965-9773(96)00048-7)
- [63] P. Chatterjee, S.P. Sen Gupta, An X-ray diffraction study of nanocrystalline titanium prepared by high energy vibrational ball milling, *Appl. Surf. Sci.* 182 (2001) 372–376, [https://doi.org/10.1016/S0169-4332\(01\)00451-2](https://doi.org/10.1016/S0169-4332(01)00451-2)
- [64] C.N.J. Wagner, J.B. Cohen, J.E. Hilliard (Eds.), *Local Atomic Arrangements Studied by X-ray Diffraction*, Gordon and Breach, New York, 1966 Chap. 7.
- [65] H.M. Otte, D.O. Welch, Formation of stacking faults in polycrystalline silicon bronze under tensile deformation, *Philos. Mag.* 9 (1964) 299–313, <https://doi.org/10.1080/14786436408229193>
- [66] D. Rafaja, C. Krbetschek, C. Ullricha, S. Martina, Stacking fault energy in austenitic steels determined using X-ray diffraction during bending, *J. Appl. Cryst.* 47 (2014) 936–947, <https://doi.org/10.1107/S1600576714007109>
- [67] C.N.J. Wagner, Stacking faults by low-temperature cold work in copper and alpha brass, *Acta Metall.* 5 (1957) 427–434, [https://doi.org/10.1016/0001-6160\(57\)90060-3](https://doi.org/10.1016/0001-6160(57)90060-3)
- [68] C.N.J. Wagner, X-ray study of low-temperature cold work in silver and aluminium, *Acta Metall.* 5 (1957) 477–482, [https://doi.org/10.1016/0001-6160\(57\)90085-8](https://doi.org/10.1016/0001-6160(57)90085-8)
- [69] M.E. Straumanis, L.S. Yu, Lattice parameters, densities, expansion coefficients and perfection of structure of Cu and of Cu-In α phase, *Acta Cryst.* A25 (1969) 676–682, <https://doi.org/10.1107/S0567739469001549>
- [70] R.W. Vook, F. Witt, Thermally induced strains in evaporated films, *J. Appl. Phys.* 36 (1965) 2169–2171, <https://doi.org/10.1063/1.1714442>
- [71] R. Adler, H. Otte, C. Wagner, Determination of dislocation density and stacking fault probability from x-ray powder pattern peak profiles, *Metall. Trans.* 1 (1970) 2375–2382, <https://doi.org/10.1007/BF03038366>
- [72] E. Schafner, M. Zehetbauer, T. Ungar, Measurement of screw and edge dislocation density by means of X-ray Bragg profile analysis, *Mater. Sci. Eng. A* 319–321 (2001) 220–223, [https://doi.org/10.1016/S0921-5093\(01\)00979-0](https://doi.org/10.1016/S0921-5093(01)00979-0)
- [73] *Jeno Gubicza, Defect Structure in Nanomaterials*, Woodhead Publishing, 2012.
- [74] A. Leineweberand, E.J. Mittemeijer, Anisotropic microstrain broadening due to compositional inhomogeneities and its parametrisation', *Zeit für Krist. Suppl.* 23 (2006) 117–122, <https://doi.org/10.1524/9783486992526-022>
- [75] U. Welzel, *Diffraction Analysis of Residual Stress; Modelling Elastic Grain Interaction*, Ph.D Thesis, Max-Planck Institute für Metallforschung, Stuttgart, Germany, 2002.
- [76] M. van Leeuwen, J.-D. Kamminga, E.J. Mittemeijer, Diffraction stress analysis of thin films: modeling and experimental evaluation of elastic constants and grain interaction, *J. Appl. Phys.* 86 (1999) 1904–1914, <https://doi.org/10.1063/1.370986>
- [77] T.P. Harzer, S. Djaziri, R. Raghavan, G. Dehm, Nanostructure and mechanical behavior of metastable Cu-Cr thin films grown by molecular beam epitaxy, *Acta Mater.* 83 (2015) 318–332, <https://doi.org/10.1016/j.actamat.2014.10.013>
- [78] J. Chakraborty, T.P. Harzer, Jazmin Duarte, Gerhard Dehm, Phase decomposition in nanocrystalline $\text{Cr}_{0.8}\text{Cu}_{0.2}$ thin films, *J. Alloy. Compd.* 888 (2021) 161391–1–161391–20, <https://doi.org/10.1016/j.jallcom.2021.161391>
- [79] J.C.M. Li, R.A. Oriani, L.S. Darken, The Thermodynamics of Stressed Solids, *Zeit. Physikalisch. Chem. Neue Folge*, Bd. 49 S. (1966) 271–290, <https://doi.org/10.1524/zpch.1966.49.3.5.271>
- [80] J. Eckert, J.C. Holzer, C.E. Krill III, W.L. Johnson, Mechanically driven alloying and grain size changes in nanocrystalline Fe-Cu powders, *J. Appl. Phys.* 73 (1993) 2794–2802, <https://doi.org/10.1063/1.353055>
- [81] J. Weertman, J.R. Weertman, *Elementary Dislocation theory*, Macmillan Ser. Mater. Sci. (1966) 173–181.
- [82] H. Suzuki, *Sci. Rep. Res. Inst. Tohoku Univ.* A 4 (1952) 452.
- [83] D. Hull, D.J. Bacon, *Introduction to Dislocations (Fifth Edition)*, Butterworth-Heinemann, 2011.
- [84] P.B. Barna, M. Adamik, Fundamental structure forming phenomena of polycrystalline films and the structure zone models, *Thin Solid Films* 317 (1998) 27–33, [https://doi.org/10.1016/S0040-6090\(97\)00503-8](https://doi.org/10.1016/S0040-6090(97)00503-8)
- [85] A. Kovács, P.B. Barna, J.L. Lábár, The nucleation and growth of intermetallic Al-Pt phases in co-deposited thin films, *Thin Solid Films* 433 (2003) 78–81, [https://doi.org/10.1016/S0040-6090\(03\)00281-5](https://doi.org/10.1016/S0040-6090(03)00281-5)
- [86] C.V. Thompson, Structure evolution during processing of polycrystalline films, *Annu. Rev. Mater. Sci.* 30 (2000) 159–190, <https://doi.org/10.1146/annurev.matsci.30.1.159>
- [87] A.H. Cottrell, C.S. Hunter, F.R.N. Nabarro, Electrical interaction of a dislocation and a solute atom, *Philos. Mag.* 44 (1953) 1064–1067, <https://doi.org/10.1080/14786441008520364>
- [88] H. Suzuki, C.S. Barrett, Deformation twinning in silver-gold alloys, *Acta Met.* 6 (1958) 156–165, [https://doi.org/10.1016/0001-6160\(58\)90002-6](https://doi.org/10.1016/0001-6160(58)90002-6)
- [89] Mary F. Doerner, W.D. Nix, Stresses and deformation processes in thin films on substrates, *Crit. Rev. Solid State Mater. Sci.* 14 (3) (1988) 225–268, <https://doi.org/10.1080/10408438808243734>
- [90] R. Huang, W. Robl, H. Ceric, T. Detzel, G. Dehm, Stress, Sheet Resistance, and microstructure evolution of electroplated Cu Films during self-annealing, *IEEE Trans. Device Mater. Reliab.* 10 (2010) 47–54, <https://doi.org/10.1109/TDMR.2009.2032768>
- [91] E. Eiper, J. Keckes, K.J. Martinschitz, I. Zizak, M. Cabie, G. Dehm, Size-independent stresses in Al thin films thermally strained down to 100 °C, *Acta Mater.* 55 (2007) 1941–1946, <https://doi.org/10.1016/j.actamat.2006.10.052>